Astrocytic NDRG2 is a potential guarder for diabetes-associated cognitive dysfunction via regulating complement C3 cascades

Tao Jiang
1. The First Affiliated Hospital of Xi'an Jiaotong University. 2. The second Affiliated Hospital of Xi'an Jiaotong University.
Yansong Li
The First Affiliated Hospital of Xi'an Jiaotong University
Shuxuan He
The First Affiliated Hospital of Xi'an Jiaotong University
Mengyu Du
The First Affiliated Hospital of Xi'an Jiaotong University
Qian Zhai
The First Affiliated Hospital of Xi'an Jiaotong University
Kairui Pu
The First Affiliated Hospital of Xi'an Jiaotong University
Meiyan Wu
The First Affiliated Hospital of Xi'an Jiaotong University
Chaoying Yan
The First Affiliated Hospital of Xi'an Jiaotong University
Zhi Ma
The First Affiliated Hospital of Xi'an Jiaotong University
Qiang Wang (dr.wangqiang@mail.xjtu.edu.cn)
The First Affiliated Hospital of Xi'an Jiaotong University https://orcid.org/0000-0002-3637-2063

Research article

Keywords: diabetes, cognitive dysfunction, NDRG2, complement C3

Posted Date: April 12th, 2022

DOI: https://doi.org/10.21203/rs.3.rs-1446406/v1

Abstract

Background

Diabetes-associated cognitive dysfunction (DACD), which mainly had three different cognitive characteristics, seriously affect the self-glycemic management and even lead to critical complications such as hypoglycemia, hyperglycemic hyperosmotic coma and ketoacidosis. As most serious stage of DACD, dementia had gradually risen to second leading cause of death in diabetes, indicating the urgency to clarify the integrative pathophysiology of DACD.

Methods

Here, Y maze and Morris water maze were used to evaluate the learning memory. Based on quantitative transcriptome sequencing and TMT proteome sequencing, we performed WGCNA analysis and GSEA analysis to demonstrate activation of complement cascades induced neurotoxic astrocyte to injury neuronal synaptic plasticity in diabetic mice. Western blotting, immunofluorescence staining, golgi staining and electrophysiology were used to verify the reliability of sequencing data.

Results

The deficiency of NDRG2 aggravated activation of complement C3 by accelerating the phosphorylation of NF-κB, ultimately lead to synaptic injury and cognitive dysfunction. Conversely, the overexpression of NDRG2 promoted remodeling of neurotoxic astrocyte by inhibiting complement C3, attenuated synaptic injury and cognitive dysfunction. Meanwhile, C3aR blockade rescued dendritic spines loss and cognitive deficits in diabetic mice. Moreover, we estimated cognitive function in diabetic or normal patients by DSST scores, which was negatively correlated with blood glucose, the level of C3 and HOMA-IR in serum.

Conclusion

Our findings illustrated the effectiveness and integrative mechanism of NDRG2-induced improving cognition from a multi-omics perspective, confirmed the expression of NDRG2 was closely related to cognitive function of diabetic mice and C3 may be a biomarker to predict the progression of DACD in human, which provided a new alerting or therapeutic strategy for patients with cognitive impairment.

Trial registration

The clinical protocol was registered and approved by the Ethics Committee of the First Affiliated Hospital of Xi'an Jiaotong University (ID: ChiCTR1900021720).

Background

The worldwide prevalence of diabetes is predicted to exceed 640 million by 2040 [1, 2]. Furthermore, the incidence of diabetes-associated cognitive dysfunction (DACD) among diabetic individuals is currently 13.1% [3] and even reaches over 24.2% in those above 75 years old [4]. DACD mainly consists of the following three cognitive characteristics: diabetes-associated cognitive decrement, mild cognitive impairment, and dementia [5]. These symptoms seriously impact self-glycemic management and may even lead to critical complications, including hypoglycemia, hyperglycemic hyperosmotic coma, and ketoacidosis. As the most serious stage of DACD, dementia had gradually risen to the second leading cause of death among individuals with diabetes [6]. Therefore, there is an immediate urgency to clarify the integrative pathophysiology of various metabolic disorders that result from diabetes.

Consolidated evidence indicates that the improvement of synaptic plasticity [7] can rescue cognitive defects in patients who are aged [8] or who have Alzheimer's disease (AD) [9]. Nonetheless, the regulatory role of astrocytic remodeling in cognitive dysfunction remains poorly understood. Each astrocyte occupies a non-overlapping region, participates in neurovascular units [10, 11], and maintains neuronal support as an active component of tripartite synapses [12]. Astrocytes secrete positive or negative glial factors to promote synaptogenesis [13, 14] or phagocytosis and pruning of synapses [15], which are processes essential for neural homeostasis related to cognition and memory [16, 17]. Classical complement signaling is activated to regulate proper synaptic formation, but control over this signaling is lost during aging and in neurodegenerative diseases [18–20]. This signaling is initiated by the activation of microglia, thus secreting C1q, Il-1α, and TNF-α, which induce the formation of the C1 complex (C1q, C1r, C1s) and cleave C4 and C2 to form C4b2b (a C3 invertase). Then, complement C3 is upregulated and cleaved into C3a and C3b [21, 22]. C3a binds with C3aR to promote microglial activation and neuronal synaptic pruning [23]. In cases of neurodegenerative disease, astrocytes acquire strong neurotoxicity [18, 24] and lose their function of promoting synaptic formation and pruning [19, 20].

As a member of the N-myc downstream regulatory gene (NDRG) family, NDRG2 is specifically expressed in astrocytes, regulating the clearance of glutamate [25] and participating in the integrity of the blood-brain barrier [26], cell proliferation[27], and differentiation [28]. The abnormal expression of NDRG2 is closely related to the pathogenesis of many neurological diseases (e.g. glioma [29], stroke [30, 31], Alzheimer’s disease [32], depression [33], and attention-deficit/hyperactivity disorder [25]). NDRG2 deficiency results in the accumulation of interstitial glutamate and increased neuroexcitatory transmission, which contributes to abnormal behaviors and impaired memory [25]. Loss of NDRG2 was found to worsen cognitive dysfunction in AD mice by reducing the levels of proteasome subunit PSMB6, which is an essential enzyme for the degradation of Aβ and tau [32]. However, the function of astrocytic NDRG2 in DACD is unknown, and whether NDRG2 is involved in the activation of complement cascades and synaptic injury requires further exploration.

In this study, we validated the negative role of astrocytic complement cascades in neuronal long-term potentiation from a multi-omics perspective. We demonstrated that astrocytic NDRG2 loss-of-function

induces the phosphorylation of NF-κB and activation of complement C3 cascades, ultimately leading to synaptic injury and cognitive dysfunction. More importantly, we found that astrocytic NDRG2 gain-of-function can promote remodeling of neurotoxic astrocytes by inhibiting p-NF-κB and complement C3. Meanwhile, we described that C3 may be a novel predictor of cognitive dysfunction in diabetic patients. This scientific discovery highlights that NDRG2 acts as both a potential guarder for reshaping the pathological structure of astrocytes and an effective intervention target for patients with neurodegenerative diseases.

Methods

Study design

Exercise is one of the five most impactful treatments for diabetes. Regular exercise has been found to promote hepatogenic factors [glycosylphosphatidylinositol-specific phospholipase D1 (Gpld1)] [8], metabolic factors (ketone bodies and lactate), and myogenic factors (Cathepsin-B and Irisin) [9], which stimulate BDNF levels [34] and improve synaptic plasticity in aged and AD patients. Here, exercise was performed in diabetic mice to accurately explore the pathogenesis of DACD. Since high intensity exercise may lead to acute diabetic complications such as ketoacidosis, seven weeks of standardized exercise at moderate intensity was carried out according to established protocols [35–37]. In the vehicle + Run and STZ + Run groups, moderate intensity exercise was performed using an animal treadmill (ZH-PT, Anhui, China). The speed parameters included a velocity of 5–8 m/min and acceleration of 4 m/s^2. Exercise was performed for 30min over five consecutive days. Vehicle and STZ groups not subjected to exercise training were free to access water and food.

Transcriptomic sequencing and WGCNA analysis

Total RNA was extracted from the hippocampi of vehicle, STZ, and Run + STZ mice using a TRIzol reagent kit. RNA quality was verified by the Nano Drop ND-1000, and RNA was reverse-transcribed to cDNA using Super Script™ II Reverse Transcriptase reagent (1896649, Invitrogen). Then cDNA was used to synthesize U-labeled second-stranded DNAs. Ultimately, 2×150bp paired-end sequencing (PE150) was performed on the Illumina Novasequencing™ 6000 (LC-Bio Technology Co., Hangzhou, China).

Weighted gene co-expression network analysis (WGCNA) of transcriptomic data was used to construct a hierarchical cluster tree, in which differently colored branches represent the 18 gene modules [38]. To satisfy the relationship of genes that conformed to scale-free topological distribution, the soft threshold β adopted a scale-free topological fitting index greater than 0.8 or the minimum β value when reaching the plateau stage. The minimum number of genes and merged cut height were set to 30 and 0.4, respectively. The PC1 of each module in PCA analysis represented module eigengene (ME), which reflected the characteristics of overall gene expression in this module. The correlation network was obtained by calculating ME correlation-ship among different modules.

TMT proteomic sequencing and GSEA analysis

TMT proteomic sequencing was performed according to previous protocols [39]. The hippocampi of vehicle, STZ, and Run + STZ mice were lysed and homogenized by SDT buffer and auto homogenizer using a velocity of 6.0 M/S three times for 30 s each [40]. After being boiled for 15 min, the samples were centrifuged at 14000g for 15 min. The filtrate was obtained from 0.22μm filters and quantified using a BCA Kit (23225, Thermo Fisher). The 20μg proteins were separated by SDS-PAGE gel for quality measurement. 200μg proteins were digested according to the instructions of Filter-Aided Sample Preparation (FASP digestion) [39]. 100μg of peptides from each sample were labeled using TMT reagent, and then fractionated by the Agilent 1260 Infinity II HPLC.

The traditional KEGG or GO analysis relied on defined difference thresholds: fold change > 1.2 or < 0.83 and p-value < 0.05. However, Gene Set Enrichment Analysis (GSEA) integrated most gene expression characteristics in the predefined gene set [41], which could detect more functional genes with no statistically significant differences. According to expression ratio, ALL genes ranked to follow the distribution of predefined gene set S were randomly distributed or concentrated at the top or bottom of the list. Here, the GSEA of transcriptomic and proteomic data was carried out in the Lian-chuan Bio-Cloud Platform. The predefined gene set was C2.Cp.KEGG.v7.1.

Animals

According to published protocols [42–44], Type 1 diabetes mellitus (T1DM) was induced in 8 to 10-week-old C57BL/6 mice weighing 21-22g. Mice were obtained from the Experimental Animal Center of Xi'an Jiaotong University and maintained under specific pathogen-free conditions with a 12-hour light-dark cycle and free access to water and food. Streptozotocin (STZ) (Sigma-Aldrich, USA) was dissolved in sterile, freshly-prepared 0.1M citric acid buffer (pH = 4.5) [45]. For five consecutive days, the diabetic mice were intraperitoneally injected with 50 mg/kg STZ while the vehicle mice were intraperitoneally injected with 0.1M citric acid buffer. After two weeks, random blood glucose was measured in the tail vein using a Roche glycemic meter. Mice with random blood glucose values greater than 16 mmol/L were considered diabetes. The fluctuations in food consumption, water intake, and body weight were recorded for the next seven weeks. C3aR antagonist was purchased from Calbiochem (catalog No. SB290157). The 16-week-old vehicle and STZ mice were intraperitoneally (i.p.) injected with PBS or C3aRA (1 mg/kg) three times per week for three weeks. According to previously studies [46, 47], mice were used for behavioral experiments at the age of 20–24 weeks, where they displayed symptoms of diabetes-associated cognitive dysfunction.

Generation of acNDRG2 KO and NDRG2 overexpression

$Ndrg2^{fl/fl}$ mice were purchased from Cyagen Biosciences, China. We performed stereotactic injection of rAAV-GFAP-CRE-WPRE-hGH into the hippocampal CA1 area of $Ndrg2^{fl/fl}$ mice, in which NDRG2 was conditionally deleted as an acNDRG2 KO, and stereotactic injection of rAAV-GFAP-EGFP-WPRE-hGH (AAV-GFP) in control group mice [48]. To achieve overexpression of NDRG2, we injected rAAV-GfaABC1D-NDRG2-2A-mCherry-WPRE-pA, AAV2/9 (AAV-NDRG2) into the hippocampal CA1 area of both vehicle and STZ mice, which gave us the vehicle + AAV-NDRG2 and STZ + AAV-NDRG2 groups. As a control, we

injected rAAV-GfaABC1D-mCherry-WPRE-SV40 pA, AAV2/9 (AAV-Ctrl) into the CA1 area of vehicle and STZ mice, which obtained vehicle + AAV-Ctrl and STZ + AAV-Ctrl mice. Stereotactic virus injection was performed according to the following steps. Mice were anesthetized with isoflurane and their heads fixed in a stereotactic apparatus (RWD, Shenzhen, China). An appropriate amount of erythromycin eye ointment was applied to the eyes to prevent conjunctival infection. A small craniotomy was performed, exposing the Bregma point of the skull. Mice were bilaterally microinjected in the following sites: anteroposteriorly (AP) -1.5mm from the Bregma point, mediolaterally (ML) ± 1mm, and dorsoventrally (DV) -1.55mm to cover the dorsal CA1. Microinjections were carried out using a 5μl syringe and a 33-gauge metal needle (65460-02, Hamilton, USA). Flow rate (24 nl/min) was controlled by an injection pump for 10min. Then, we stopped the needle, waited for an additional 10min to allow the viral vector to diffuse away from the needle track, and slowly withdrew the needle over the course of another 5min. After suturing the incision, mice recovered on an electric blanket for postoperative care.

Golgi staining

After various experimental treatments, mouse brains were collected and fixed in 4% paraformaldehyde for 24h. The hippocampus was cut into 2-3mm blocks and immersed in Golgi solution for 48h – Golgi solution was changed once every three days for a total of 14 days. Then, samples were dehydrated in 15% sucrose solution for one day and 30% sucrose solution for two days at 4℃ in dark conditions. After treatment with concentrated ammonia water and fixing solution, samples were further dehydrated for two to three days, then frozen and sliced into 100μm sections which were sealed with glycerin gelatin. Images were captured as soon as possible using a super-resolution confocal microscope (Leica TCS SP8 STED 3X) with 20X or 200X magnification. We performed Sholl analysis to examine total dendritic length and neuronal complexity. We used Imaris analysis to reconstruct the 3D structure of dendritic spines by automatic classification.

Electrophysiology

We performed analysis of miniature excitatory postsynaptic currents (mEPSCs) to observe neuronal synaptic transmission [49]. After being anesthetized by isoflurane, mice were subjected to perfusion with an oxygenated (95% O_2/5% CO_2) cutting solution consisting of the following reagents: 2.5 mM KCl, 120 mM choline chloride, 7 mM $MgCl_2$, 1.25 mM NaH_2PO_4, 0.5 mM $CaCl_2$, 5 mM sodium ascorbate, 26 mM $NaHCO_3$, 3 mM sodium pyruvate, and 25 mM glucose. Then, mice brains were prepared into 300 μm hippocampal slices using a VT1200S Vibratome (Leica Microsystems). Slices were transferred into cutting solution at 34°C for 15 min and translocated into the incubator with artificial cerebrospinal fluid (ACSF), which contained 2.5 mM KCl, 124 mM NaCl, 2 mM $MgSO_4$, 1.25 mM NaH_2PO_4, 2.5 mM $CaCl_2$, 10 mM glucose, and 26 mM $NaHCO_3$. Slices were incubated at 25 ± 1°C for at least one hour. Whole-cell patch-clamp recordings of CA1 pyramidal neurons were conducted at -70 mV in the presence of 100 μM picrotoxin and 1 μM TTX for mEPSC recording. The pipette solution contained the following reagents: 5 mM KCl, 125 mM K-gluconate, 10 mM HEPES, 1 mM $MgCl_2$, 0.2 mM EGTA, 4 mM Mg-ATP, 0.3 mM Na-GTP, and 10 mM phosphocreatine (pH 7.35, 290 mOsm). Signals were acquired using a MultiClamp 700B

amplifier and 1550A digitizer (Molecular Devices). To obtain a high signal-to-noise ratio and accurately determine the mEPSC amplitude, only events > 10 pA were accepted for analysis [50]. Data were collected with pClamp10.0 software (Molecular Devices).

Transmission electron microscopy

The ultrastructure of postsynaptic density (PSD) was identified by transmission electron microscopy. After experimental treatment, mice were subjected to cardiac perfusion with 2% paraformaldehyde + 2% glutaraldehyde solution, which was precooled at 4°C. The hippocampus tissues were cut into 2×1×1 mm block and immersed in 4% glutaraldehyde. Then, samples were rinsed two times with 0.2 mol/L phosphate buffer solution for 30 min each and fixed with Osmium acid for 2 h. The samples were dehydrated in a graded fashion using 50%, 70%, 80%, 90%, and 100% ethanol for 15 minutes at each concentration, then embedded on epoxy resin to make 40-50nm ultra-thin slices on copper mesh. Imaging was performed with a Hitachi H-7650 transmission electron microscope (Hitachi, Japan).

Y-maze

Y-maze (30cm×6cm×15cm) testing was used to evaluate spatial working memory [51]. The maze consisted of an isolated triangular central area and three identical arms each at an angle of 120°. The mice were allowed to freely explore the Y-maze for 8min. If they could accurately remember the directions in which they came from, the correct alternation order was ABC or another sequence of three non-repeated arms. If they were not able to remember these directions, the alternation order would include at least two repeated arms (i.e., ABB, ABA, ACA, or ACC). Therefore, spontaneous alternation (%) was calculated using the following equation: spontaneous alternation (%) = correct alternation / (total arm entries − 2) ×100. Meanwhile, the total arm entries and total distance parameters reflected autonomous movement ability. To ensure consistent and reliable experimental data, the surrounding environment was kept quiet and the experiment was performed during the same period of each day.

Morris water maze (MWM)

The Morris water maze consisted of a thermostatic swimming pool at a temperature of 20–25°C. Four different shapes (circle, square, diamond, and triangle) were pasted on the four sides of the maze. A hidden platform was located 0.5 cm lower than the surface of the water in the fourth quadrant. During the five training days, mice were gently placed into water from the four marked directions. Escape latency to the hidden platform and swimming velocity were recorded using a WMT-100 Morris system. On the last day, the hidden platform was removed. The number of platform crossovers and target quadrant retention time (%) were observed to evaluate spatial learning memory [52].

Western blotting

According to the established protocol, the hippocampal samples were harvested and weighed (0.015-0.02g), then homogenized in 150-200ul of fresh ice-cold RIPA lysis buffer (Beyotime, Nantong, China) which contained protease inhibitor and phosphatase inhibitor. The samples were stirred by an electric grinder for 3s × 4 times on the ice, crushed with an ultrasonic cell crusher for 4s × 4 times, and

centrifuged at 12000 rcf for 10min. The supernatant was taken for protein quantification and diluted to a protein concentration of 3 ug/ul. The following primary antibodies were used: anti-C3 rabbit monoclonal antibody (ab200999, Abcam, UK), anti-PSD95 mouse monoclonal antibody (ab13552, Abcam, UK), anti-Syp rabbit monoclonal antibody (ab32127, Abcam, UK), anti-NDRG2 rabbit monoclonal antibody (5667-WB, CST, USA), anti-NF-κB rabbit monoclonal antibody (ab32536, Abcam, UK), anti-p-NF-κB rabbit monoclonal antibody (3033T, CST, US), and anti-β-tubulin mouse monoclonal antibody (66240-1-lg, Proteintech, China).

Immunofluorescence staining and ELISA

After being gradient dehydrated by 20% and 30% glucose, brains were embedded with OCT glue and frozen in a cryostat (Cryostar NX50™, Thermo Scientific) for over one hour. The frozen brain were prepared into 16μm thick sections, then incubated with goat serum containing 0.2%Trion-100 at 37℃ for 30min. NDRG2 labeling was performed by incubating with primary anti-NDRG2 rabbit monoclonal antibody (ab174850-IF, Abcam, UK), anti-GFAP chicken polyclonal antibody (GTX85454, Gene Tex, USA), and anti-NeuN mouse monoclonal antibody (MAB377, Merck Millipore, USA) overnight at 4℃. The sections were washed with PBS (phosphate-buffered saline) for 7min × 3 times. The next day, sections were incubated for 2h in fluorescent secondary antibodies Alexa Fluor®488 (139424, Jackson Immuno, USA), Alexa Fluor® 594 (ab150064, Abcam, UK), and Alexa Fluor® 647 (ab150115, Abcam, UK). DAPI was added during the final 5min of incubation. The sections were stored at 4℃ until observed, and images were captured as soon as possible using a confocal fluorescence microscope (BX51, Olympus, Tokyo, Japan) or super-resolution confocal microscope (Leica TCS SP8 STED 3X). Insulin concentration was detected according to the instructions of a Mouse INS (Insulin) ELISA Kit (E-EL-M1382c) purchased from Elabscience, Wuhan, China.

Subjects and clinical assessments

To analyze the possible risk factors of diabetes-associated cognitive dysfunction in humans, we recruited 40 subjects consisting of 27 diabetic individuals (17 male and 10 female, mean age 68.963 years) and 13 non-diabetic individuals (10 male and 3 female, mean age 66.6923 years). The inclusion criteria were those over 60 years of age who either met the clinical diagnostic criteria for diabetes or did not (healthy controls) from the First Affiliated Hospital of Xi'an Jiaotong University. We excluded patients affected by infection or inflammation or who had other clinically diagnosed mental disorders. We assessed cognitive function using DSST scores [53, 54] and collected serum and metabolic indicators for correlation analysis. The Human C3 (Complement Component 3) ELISA Kit (E-EL-H6054) and Human INS(Insulin) ELISA Kit (E-EL-H2665c) were purchased from Elabscience, Wuhan, China. Measurements of C3 and insulin were performed according to the manufacturer's instructions.

Statistical analysis

GraphPad Prism Version 7.0 software was used for statistical analysis. All values were expressed as mean ± SEM unless otherwise stated and were performed Normality test. Comparisons between groups were analyzed using a two-tailed Student's t-test. The escape latency in the MWM test and the fluctuation

of body weight were analyzed by two-way ANOVA and Tukey's multiple comparisons test. The associations between risk factors and DSST scores were assessed using logistic regression. Other values were analyzed by one-way ANOVA with Tukey's multiple comparisons test. * P≤0.05, ** P≤0.01, *** P≤0.001, **** P≤0.0001, $^{\#}$ P≤0.05, and $^{\#\#}$ P≤0.01 were considered statistically significant.

Results

Cognitive dysfunction and impairment of neuronal synaptic plasticity were presented in diabetic mice

To validate the cognitive dysfunction of diabetes, we assessed metabolic signs, behavioral alterations, and neuronal morphology & function in diabetic and non-diabetic mice (Fig. 1A). Random blood glucose level, food & water intake, and HOMA-IR value were higher in diabetic mice compared to non-diabetic mice. Body weight was clearly lower in the diabetic group compared to the non-diabetic group at baseline, but this observation was reversed by exercise (Fig. 1B-C and Fig. S1A-D). Furthermore, we performed Y-maze and Morris water maze (MWM) behavioral tests to observe learning memory defects in diabetic mice. The alternation triplet (%) was decreased in diabetic mice, whereas exercise improved the alternation triplet (%) in STZ + Run mice (Fig. 1D). Meanwhile, there were no statistically significant differences in Y-maze total arm entries or total distance between each group (Fig. S1E-F). In the MWM test, escape latency was delayed in diabetic mice, while platform crossover and target quadrant retention time (%) were decreased in the STZ group. All of these deficiencies were rescued by exercise in the STZ + Run group (Fig. 1E-G). There were no significant differences in swimming velocity between each of the groups (Fig. S1G). Together, these results indicate that exercise alleviated abnormal metabolic signs and improved hippocampal-dependent learning memory in diabetic mice.

To observe the neuronal morphology of diabetic mice, we evaluated neuronal complexity and classified the 3D structure of dendritic spines. Both the total dendritic length and neuronal complexity were lower in diabetic compared to non-diabetic mice, which were preserved after exercise in STZ + Run mice (Fig. S2A-C). The reconstruction of dendritic spines demonstrated that total spine density was obviously reduced in diabetic mice, especially in stubby and mushroom spines but with exception for filopodia and long thin spines. Exercise (STZ + Run group) was found to increase total spine density in stubby and mushroom spines (Fig. 1H-K and Fig. S2D-E). Meanwhile, we also examined how diabetes impacted the expression of synaptic proteins. The expression levels of excitatory postsynaptic density marker PSD-95 and presynaptic density marker SYP were decreased in diabetic compared to non-diabetic mice, and this deficit was rescued by exercise in STZ + Run mice (Fig. S1H-I). Consistent with the alteration of neuronal morphology and dendritic spine density, the frequency of mEPSCs were abnormally elevated in diabetic compared to non-diabetic mice, which was an effect obviously attenuated by exercise (Fig. 1L-N). However, there was no difference in the amplitude of mEPSCs between the groups (Fig. 1O-P). The ultrastructure observed via electron microscopy showed the representative diagrams of synapse counts per 27.68μm^2 and PSD length & thickness in the hippocampus (Fig. S2F). The synapse count per

27.68μm^2 was lower in diabetic mice (four) compared to vehicle mice (eight), where this deficit was again rescued by exercise (Fig. S2G). Exercise restored the reductions of PSD length and thickness in diabetic mice (Fig. S2H-I). More specifically, PSD length ranged from 200 nm to 400 nm in vehicle mice, but it decreased to between 100 nm and 250 nm in diabetic mice. PSD length was increased to normal levels in STZ + Run mice (200–350 nm) (Fig. S2J). PSD thickness ranged from 40 nm to 120 nm in vehicle mice, decreasing to between 20 nm and 60 nm in diabetic mice. Once again, PSD thickness was increased to relatively normal levels (40–80 nm) in STZ + Run mice (Fig. S2K). Above all, our findings illustrate that exercise ameliorated many of the impairments in synaptic plasticity and cognition in diabetic mice.

Transcriptomic and proteomic analysis revealed the potential role of astrocytic NDRG2 and complement cascades in regulating neuronal synaptic plasticity at diabetic mice

To illustrate the integrative regulatory mechanism of neurons, astrocytes, and microglia, we analyzed hippocampal tissue from the vehicle, STZ, and STZ + Run groups for quantitative transcriptomic sequencing. The mRNA transcripts were processed using String Tie and ballgown (http://www.bioconductor.org/packages/release/bioc/html/ballgown.html) to arrive at 55,450 total genes. We identified 2,664 differentially-expressed genes by filtering with fold change > 2 or < 0.5 and p-value < 0.05 in DESeq2 analysis (http://www.bioconductor.org/packages/release/bioc/html/DESeq2.html). PCA analysis of the 15 samples indicated that the distributions of samples among the three groups were discrete and obviously different from each other, whereas the distribution of samples within each group was aggregative and showed great consistency (Fig. S3A). Next, we performed weighted gene co-expression network analysis (WGCNA) of the 55,450 total genes from the 15 independent samples. A soft threshold of 0.8 and merged cut height of 0.4 were used to ensure that the gene correlation network satisfied scale-free-topological distribution. From WGCNA, we obtained a cluster dendrogram with 18 modules (Fig. 2A). PCA analysis of the 18 modules confirmed that the distribution of the modules was dispersed, representing different groups of genes based on biological function (Fig. S3B). PC1 values reflected weighted gene expression patterns in each module, which was called the module eigengene value. We identified hub genes and biological functions according to the weighted value of each gene and Gene Ontology (GO) enrichment analysis of each module [38]. Then, we clarified the cellular nature of each module by checking whether it consisted of particular cell-type biomarkers [55].

We observed enrichment of neuronal synaptic plasticity genes – Syt1, Manf, Syp and Bdnf – in module 1 (Fig. 2C). The module eigengene for module 1 was clearly decreased in diabetic mice, and it was moderately improved after exercise (Fig. S3C). We also saw enrichment of astrocytic and oligodendrocytic genes – Lcn2, Ndrg2 and Mobp – in module 2 (Fig. 2D). Furthermore, we found the relationships between each module and identified a highly negative relationship between module 1 and module 2, which reflected that astrocytic and oligodendrocytic genes play a negative role in the neuronal synaptic plasticity of diabetic mice (Fig. 2B). Moreover, endoplasmic reticulum and immune response genes – Cxcr1 and Cxcl11 – were enriched in module 4 (Fig. S3D), which had a negative correlation with module 1 and positive correlation with module 2, thus forming a trilaterally logic-reasonable relationship.

Characterized by having the most abundant genes, astrocytic inflammatory response genes were enriched in module 17 (Fig. S3E). Hub genes related to complement activation of microglia – Klf17, C1s2, and F3 – were enriched in module 8, whereas genes associated with complement and coagulation cascades, including Fga, F9, Cxcr2, and Fgg, were enriched in module 11 (Fig. S3F-G). We identified positive relationships between module 17, module 8, and module 11 (Fig. 2B), which reflected the biological mechanism that complement activation of microglia, astrocyte inflammatory response, and complement & coagulation cascades are intimately linked with each other. Specifically, microglia-derived C1q, TNFα, and Il-1α work together to induce A1 reactive astrocytes, then upregulate the expression of astrocytic C3 to initiate complement & coagulation cascades, which causes astrocytes to lose their protective function of promoting synaptic formation and acquire strong neurotoxicity, thus injuring neuronal synaptic plasticity.

KEGG enrichment analysis of the 2,664 differentially expressed genes included the PI3K − Akt signaling pathway, MAPK signaling pathway, Glutamatergic synapse, and Neuroactive ligand − receptor interaction terms (Fig. S3H). However, to ignore the influence of thresholds on differentially expressed genes, we used gene set enrichment analysis (GSEA) to screen out the most biologically significant gene sets. In diabetic mice, the MAPK signaling pathway concentrated at bottom of the ranked list (P = 0.0003, STZ vs. vehicle) and the normalized enrichment score (NES) was found to be -1.69. Conversely, this pathway concentrated at top of the list (P = 0.0014, STZ + Run vs. STZ, NES = 1.53) in STZ + Run mice. These results were closely correlated with the injury of neuronal synaptic plasticity in the WGCNA analysis of diabetic mice, which reversed after exercise (Fig. S4A). The neuroactive ligand receptor interaction pathways enriched at the top of the ranked list in diabetic mice compared to vehicle mice (P = 0.0251, STZ vs. vehicle, NES = 1.41), and concentrated at bottom of the ranked list in STZ + Run mice (P = 0.0086, STZ + Run vs. STZ, NES=-1.50). This finding reflects the upregulation of neuroactive ligand receptor interaction in diabetic mice and subsequent downregulation following exercise (Fig. S4B).

Proteins are the ultimate executors in life activities and animal behaviors [56]. To validate the correlation network of RNA-sequencing, we analyzed the results of TMT-labeled proteomic sequencing of hippocampus tissue in vehicle, STZ, and STZ + Run mice, with three independent biological duplicates in each group. We selected the Uniprot_MusMusculus_17027_20200226 database for qualitative analysis and acquired 295,274 total spectra with 114,660 peptide spectra matches, screening out 53,640 unique peptides and 6,557 proteins. PCA analysis illustrated that the distribution of samples was discrete among groups and concentrated within each group (Fig. S5A). The threshold used for differentially expressed proteins were fold changes > 1.2 or < 0.83 accompanied by a p-value < 0.05. We detected 151 upregulated proteins and 29 downregulated proteins in diabetic mice, whereas a volcano plot showed six upregulated proteins and 78 downregulated proteins in STZ + Run mice (Fig. S5B-D). The results of proteomic GSEA were consistent with correlation network analysis of RNA-sequencing, which involved complement coagulation cascades and long-term potentiation pathways. The complement and coagulation cascades enriched at the top of the ranked list in STZ mice compared to vehicle mice (P = 0.0002, STZ vs. vehicle, NES = 2.22). Furthermore, these cascades concentrated at the bottom of the list in STZ + Run mice (P = 0.0035, STZ + Run vs. STZ, NES=-1.82). Overall, these findings reflect the upregulation of complement

and coagulation cascades in diabetic mice and subsequent downregulation following exercise (Fig. 3A). The long-term potentiation pathways were enriched at the bottom of the ranked list in diabetic mice (P = 0.0445, STZ vs. vehicle, NES=-1.40), and at the top of the list in the STZ + Run group (P = 0.0041, STZ + Run vs. STZ, NES = 1.69). These results are consistent with WGCNA analysis, which had shown that injury in neuronal synaptic plasticity occurred in diabetic mice and was reversed after exercise (Fig. 3B). The expression levels of C3, FGA, FGG, and FGB proteins involved in complement and coagulation cascades, as well as proteins involved in long-term potentiation pathways, are illustrated in the heat map (Fig. 3C-D).

Although omics provided details for an integrated mechanism from a macro perspective, it was also critical to verify the reliability of our results at a micro level. Accordingly, the expressions of complement C3 and astrocytic NDRG2 were examined by western blotting and immunostaining. As a key node in complement cascades, we found that C3 expression levels were increased in diabetic mice and decreased following exercise (Fig. 3E-F), suggesting that astrocytes were activated into their neurotoxic A1 form in diabetic mice and attenuated after exercise. Then, we sought to assess the expression of astrocytic marker NDRG2. We found that NDRG2 levels were decreased in the STZ group compared to vehicle mice, but exercise led to a significant increase in the expression of NDRG2 (Fig. 3E-G). Meanwhile, immunofluorescence staining was performed by confocal microscopy to observe the intensity of C3 and NDRG2. We observed that NDRG2 mainly colocalized with astrocytic maker GFAP, but not with neurons, in the hippocampus. Consistent with western blotting results, the confocal intensities of C3 in the STZ groups were increased than that of the vehicle groups, and the intensities of NDRG2 in the STZ groups were weaker than that of the vehicle groups, which were all rescued by exercise (Fig. S5E and Fig. S6).

NDRG2 deficiency accentuated dendritic spine loss and cognitive dysfunction by activating p-NF-κB/C3 signaling

$Ndrg2^{fl/fl}$ mice were obtained in which NDRG2 was conditionally deleted in a Cre-mediated pattern. To acquire astrocyte-specific conditional NDRG2 knockout mice (acNDRG2 KO), we injected rAAV-GFAP-CRE-WPRE-hGH into the hippocampi of $Ndrg2^{fl/fl}$ mice, and also injected rAAV-GFAP-EGFP-WPRE-hGH (AAV-GFP) into another group to serve as a control (Fig. 4A) [48]. We validated acNDRG2 KO by western blotting and immunostaining, with the results showing an absence of NDRG2 in the astrocytes (Fig. 4B-C and E). The expression levels of C3 and p-NF-κB were increased in acNDRG2 KO + Run + STZ mice compared to control + Run + STZ mice (Fig. 4C-D and F-G). The results of the classification of dendritic spines showed that acNDRG2 KO mice experienced an accelerated reduction of stubby, mushroom, and long thin spine density, as well as total spine density, compared to control + Run + STZ mice (Fig. 4H-M). Although no significant differences in the escape latency were observed between the acNDRG2 KO and control groups (Fig. 4N), the platform crossover and target quadrant retention time (%) were decreased in the acNDRG2 KO + Run + STZ group (Fig. 4O-P). Above all, NDRG2 deficiency was found to promote abnormal NF-κB activation. As an astrocytic target of p-NF-κB, this led to complement C3 being aberrantly released, thus impairing dendritic spines and cognitive function in diabetic mice.

Overexpression of NDRG2 alleviated damages to synaptic structure and cognitive dysfunction by inhibiting p-NF-κB/C3 signaling

Although we confirmed that complement C3 levels were increased in diabetic mice and more seriously elevated after astrocytic NDRG2 loss-of-function, we sought to find a better intervention to reduce the production of C3 at its source. To accomplish this, we investigated the effects of NDRG2 overexpression, which included a remodeling of the pathological structure of astrocytes to inhibit the production of C3. We then clarified the effectiveness of rAAV-GfaABC1D-NDRG2-2A-mCherry-WPRE-pA, AAV2/9 (AAV-NDRG2), finding that the expression of NDRG2 was elevated in the vehicle + AAV-NDRG2 and STZ + AAV-NDRG2 groups (Fig. 5A-C). Consistent with our previous results, the levels of NDRG2 were decreased in the STZ + AAV-Ctrl group compared to the vehicle + AAV-Ctrl group. The overexpression of NDRG2 downregulated heightened levels of p-NF-κB and C3 in diabetic mice (Fig. 5D-F), indicating that a gain-of-function in NDRG2 could inhibit complement signaling and neurotoxic characteristic.

Working memory and spatial memory were assessed using Y-maze and MWM testing. Although there were no significant differences in Y-maze total arm entries and total distance among the four groups, the alternation triplet (%) was decreased in the STZ + AAV-Ctrl group compared to the vehicle + AAV-Ctrl group, and was increased with overexpression of NDRG2 in the STZ + AAV-NDRG2 group (Fig. 5G and Fig. S7A-B). In the MWM tests performed at three to five days, escape latency was delayed in the STZ + AAV-Ctrl group compared to the vehicle + AAV-Ctrl group, whereas NDRG2 overexpression clearly shortened escape latency in the STZ + AAV-NDRG2 group (Fig. 5H). There were no significant differences in swimming velocity between the groups (Fig. S7C). Platform crossover and target quadrant retention time (%) were decreased in the STZ + AAV-Ctrl group compared to the vehicle + AAV-Ctrl group, and this deficit was rescued in the STZ + AAV-NDRG2 group (Fig. 5I-J). These results indicate that NDRG2 overexpression improves hippocampal-dependent memory in diabetic mice.

The expression levels of PSD95 and SYP were decreased in the STZ + AAV-Ctrl group compared to the vehicle + AAV-Ctrl group, but NDRG2 overexpression improved protein levels in the STZ + AAV-NDRG2 group (Fig. 5K-L). The automatic classification of dendritic spine density demonstrated that overexpression of NDRG2 reversed the reductions in stubby, mushroom, and total spine densities in diabetic mice, but did not significantly impact long thin or filopodia spine density (Fig. 6A-F). Representative ultrastructure images describing PSD length, thickness, and synapse counts in the hippocampus were obtained via electron microscopy and shown in 10K and 25K (Fig. S7D). The synapse count per 27.68μm^2 was reduced from 7.25 in the vehicle + AAV-Ctrl group to 3.3 in the STZ + AAV-Ctrl group, and it was increased to normal in the STZ + AAV-NDRG2 group (Fig. S7E). PSD length and thickness were reduced in the STZ + AAV-Ctrl group compared to the vehicle + AAV-Ctrl group, whereas NDRG2 overexpression restored both PSD length and thickness (Fig. S7F-G). More specifically, PSD length ranged from 150 nm to 400 nm in the vehicle + AAV-Ctrl group, decreased to 50–300 nm in the STZ + AAV-Ctrl group, and was restored to 150–400 nm in the STZ + AAV-NDRG2 group (Fig. S7H). PSD

thickness ranged from 40 nm to 80 nm in the vehicle + AAV-Ctrl group, decreased to between 20 nm and 40 nm in the STZ + AAV-Ctrl group, and was increased to 20–60 nm in the STZ + AAV-NDRG2 group (Fig. S7I). Above all, these findings indicate that NDRG2 overexpression protected diabetic mice from cognitive defects and neuronal synaptic injury.

C3aR antagonist rescued dendritic spine loss and cognitive dysfunction in diabetic mice

We illustrated that abnormally high C3 levels induced synaptic injury of neighboring neurons. Then, we used C3aR antagonists to clarify whether C3aR blockade could rescue dendritic spine loss and cognitive deficits in diabetic mice (Fig. 7A). The Y-maze alternation triplet (%) was decreased in STZ + PBS mice compared to vehicle + PBS mice, while C3aR blockade improved the alternation triplet (%) in the STZ + C3aRA group (Fig. 7B). There were no significant differences in total arm entries or total distance between each group (Fig. 7C-D). In the MWM tests, C3aR antagonist was found to reverse both delayed escape latency and lower platform crossover in the STZ + C3aRA group compared to STZ + PBS mice (Fig. 7E-F). Automatic classification of dendritic spines proved that C3aR blockade reversed the reduction of total spine density, particularly regarding mushroom and stubby spines, in STZ + C3aRA mice compared to the STZ + PBS groups (Fig. 7G-L). Taken together, these results indicate that C3aR antagonist treatment rescued cognitive impairment and restored synaptic refinement in diabetic mice.

Complement 3 may be a predictor for cognitive dysfunction in diabetic patients

In mice with diabetes-associated cognitive dysfunction, we observed significantly increased levels of C3 in the hippocampus, which induced synaptic spine loss and cognitive deficits. As an extension of these results, we wanted to see if there were any differences in cognitive function between diabetic and normal patients, and if so, what the predictive factors were. To accomplish this, we collected the serum and metabolic indicators from 13 non-diabetic and 27 diabetic patients, then assessed cognitive function using the Digit Symbol Substitution Test (DSST) scoring system [53, 54]. We observed no differences between the two groups regarding baseline clinical data, such as age (66.69 ± 4.211 y in non-diabetic and 68.96 ± 4.95 y in diabetic patients), BMI (22.99 ± 2.049 in non-diabetic and 24.08 ± 2.476 in diabetic patients), systolic blood pressure, and diastolic blood pressure (Fig. 8D-G). However, the average DSST score of diabetic patients (22.04 ± 9.263) was significantly lower than that of non-diabetic peers (38.31 ± 8.31) (Fig. 8A). Although given standard glycemic control, the fasting blood glucose of diabetic patients (6.889 ± 1.682 mmol/L) was higher than that of non-diabetic patients (4.618 ± 1.166 mmol/L) (Fig. 8B). Additionally, the insulin resistance index HOMA-IR of diabetic patients was 1.803 times higher than that of non-diabetic patients (Fig. 8C). We found that DSST score was negatively correlated with fasting blood glucose (r = -0.4356, P = 0.0050) and HOMA-IR value (r = -0.3469, P = 0.0283) (Fig. 8I-J). More importantly, levels of complement C3 in human serum were elevated in diabetic patients (1.506 ± 0.6155 mg/mL) compared to non-diabetic patients (0.9587 ± 0.457 mg/mL) (Fig. 8H). Furthermore, cognitive DSST score

was negatively correlated with C3 level (r = -0.3315, *P* = 0.0366) (Fig. 8K). These results demonstrate that higher levels of serum C3 are associated with cognitive deficits in diabetic patients, and that C3 may be an alerting marker for diabetes-associated cognitive dysfunction in humans.

Discussion

In this study, we analyzed the integrative pathogenesis of DACD by conducting transcriptomic and TMT quantitative proteomic sequencing of hippocampal tissue from diabetic mice, which revealed that the activation of complement cascades accelerated impairment of neuronal synaptic plasticity. We report that NDRG2 acts as a regulator of astrocytic-neuronal interaction via NF-κB/C3/C3aR signaling to restore synaptic function in diabetic mice (Fig. 9).

We performed WGCNA of the transcriptome and classified 18 modules in a cluster dendrogram. Module 1 was enriched in genes related to neuronal synaptic plasticity, module 2 was enriched in Ndrg2 and Lcn2 genes related to astrocytes, modules 4 & 17 were enriched in endoplasmic reticulum and astrocytic inflammatory response genes, and modules 8 & 11 were enriched in complement cascade genes. We then determined the relationships between each module, identifying a highly negative correlation between module 1, module 2, and module 4, which reflected the negative relationship between astrocytic inflammatory response and neuronal synaptic plasticity in diabetic mice. Consistent with our results, WGCNA from a large proteomic study on AD brain and cerebrospinal fluid demonstrated that AD pathology and cognitive dysfunction was correlated with Module 4 sugar metabolism, which consisted of proteins linked to astrocytic and microglial activation [55]. We also identified positive correlations between module 17, module 8, and module 11, which suggested that activated microglia promoted astrocytes to secrete large amounts of C3, thus amplifying complement cascades and immune inflammation and ultimately leading to impairment of synaptic plasticity [57]. In the neurodegenerative diseases, C3 has strong neurotoxic properties and mediates overactivation of the complement cascade, which damages synaptic structures and matured oligodendrocytes [58, 59].

Furthermore, GSEA of proteomic sequencing results demonstrated that the complement cascade pathway was overactivated in diabetic mice, and it was accompanied by significant upregulation of complement C3 and downregulation of long-term potentiation related proteins, such as those within the MAPK and CaMK families. From a microscopic perspective, we classified the 3D structures of dendritic spines, identified the ultrastructure of postsynaptic density (PSD), and induced miniature excitatory postsynaptic currents (mEPSCs) to observe synaptic transmission, which all illustrated impairment of neuronal synaptic plasticity. Since the microbiota-metabolites-brain axis [60] and neuronal mitochondrial abnormalities [61] are known to be involved in the cognitive dysfunction of diabetic mice, we assessed the secretion of C3, which succeeds to impair neuronal synaptic plasticity and memory loss [62]. We found that C3 levels were significantly increased in diabetic mice and decreased after exercise. Moreover, we verified that the expression levels of NDRG2, PSD95, and SYP, which alter the neurotoxicity of astrocytes, were significantly decreased in diabetic mice, where these deficits were reversed by exercise.

In summary, we conducted transcriptomic and proteomic sequencing to reveal that astrocytic NDRG2/C3 has a vital role in neuronal synaptic plasticity.

Astrocytes are the primary secretory source of C3 [19], and NDRG2 is specifically expressed in astrocytes [63]. The deficiency of NDRG2 is closely related to the pathogenesis of attention-deficit/hyperactivity disorder and memory impairment [25], and has also been found to aggravate cerebral ischemic injury [30] and cognitive impairment in Alzheimer's disease [32]. Additionally, previous research has shown that loss of NDRG2 altered astrocytic morphology and neuronal communication by regulating the accumulation of the Rho-GTPase pathway [64]. Furthermore, deletions of the 14q11.2 chromosome, which encodes NDRG2 genes associated with neurite outgrowth, in three children resulted in developmental delay, cognitive impairment, and facial anomalies [65]. To further explore whether NDRG2 is involved in the activation of complement cascades and synaptic injury, we performed conditional astrocytic NDRG2 knockout. The deficiency of NDRG2 was found to promote phosphorylation of NF-κB and induce abnormal NF-κB activation, thus accelerating the expression of C3 and complement cascades and ultimately leading to dendritic spine loss and cognitive dysfunction. It has been reported that the complement C3 promoter includes two κB binding sites and that direct binding of NF-κB to the C3 promoter can initiate transcription of C3, as validated by chromatin immunoprecipitation [20]. This finding reflects that C3 acts as a direct NF-κB target within astrocytes. Furthermore, we found that the overexpression of NDRG2 could promote remodeling of neurotoxic astrocytes by inhibiting p-NF-κB and complement cascades. In addition, NDRG2 overexpression increased the expression of synaptic proteins PSD95 & SYP, dendritic spine density, synaptic counts, and the distribution of PSD length & thickness, thus attenuating synaptic injury and cognitive deficits in diabetic mice. These results confirm that the expression of NDRG2 is closely related to the cognitive function of diabetic mice, regulating the activation of complement cascades by inhibiting p-NF-κB.

In the processes of aging and the neurodegenerative diseases, microglia and astrocytes have been found to be the main sources to secrete complement component, while neurons, endothelial cells, and oligodendrocytes act as additional contributors. Furthermore, C3aR is expressed in neurons, vascular endothelial cells, and microglia [58, 66]. Here, we report that C3aR blockade was able to rescue dendritic spine loss and impaired cognition in diabetic mice, reflecting the integrated molecular mechanism that abnormally high C3 levels act on C3aR to induce synaptic injury. Moreover, the hyperglycaemia, microangiopathy, and macroangiopathy of diabetic patients contribute to executive dysfunction as well as mental and motor slowing [67]. The levels of C1q and C3 have been shown to be significantly increased in the brain tissue of AD patients [19], and the expression levels of C3 in cerebrospinal fluid were significantly upregulated in AD patients [68]. RNA sequencing analysis of human hippocampus tissue has illustrated that the levels of C3/C3aR are closely associated with the diagnosis of dementia [69]. In our work, we collected the serum of 13 non-diabetic and 27 diabetic patients and evaluated cognitive function using DSST scores. We identified negative relationships between fasting blood glucose & HOMA-IR and cognitive function of diabetic patients. More importantly, DSST scores were negatively correlated with C3 levels. These results indicate that higher levels of serum C3 are associated with cognitive deficits in diabetic patients, meaning that C3 may be a predictor of cognitive dysfunction in

diabetic patients. However, muti-center clinical studies are needed to confirm these results and obtain more accurate and universal conclusions. Consistent with our results, the Mini-Mental State Examination scores for diabetic patients have been shown to be lower than those of non-diabetic patients in all domains except for attention and language, and serum S100B levels were positively associated with cognitive function in diabetic patients [70].

Conclusions

Our scientific discovery not only demonstrates the effectiveness and integrative mechanism of NDRG2 to improve cognitive function from a multi-omics perspective, but also confirms the beneficial effects of NDRG2 from a micro perspective. The overexpression of astrocytic NDRG2 inhibited the over-activation of complement cascades mediated by C3 protein, thus alleviating cognitive dysfunction in diabetic mice. Our findings highlight the potential of NDRG2 targeting as an effective intervention to reshape the pathological structure of astrocytes in neurodegenerative diseases, and also suggest that C3 may be used as an alerting marker for diabetes-associated cognitive dysfunction in humans.

Abbreviations

AP
Anteroposteriorly
ACSF
Artificial cerebrospinal fluid
AAV-GFP
rAAV-GFAP-EGFP-WPRE-hGH
acNDRG2 KO
Astrocyte-specific conditional NDRG2 knockout mice
AAV-Ctrl
rAAV-GfaABC1D-mCherry-WPRE-SV40 pA, AAV2/9
AAV-NDRG2
rAAV-GfaABC1D-NDRG2-2A-mCherry-WPRE-pA, AAV2/9
C3
Complement Component 3
DACD
Diabetes-associated cognitive dysfunction
DV
Dorsoventrally
GSEA
Gene Set Enrichment Analysis
Gpld1
Glycosylphosphatidylinositol-specific phospholipase D1

ML
Mediolaterally
ME
Module eigengene
MWM
Morris water maze
mEPSCs
Miniature excitatory postsynaptic currents
NDRG2
N-myc downstream regulatory gene 2
PSD
postsynaptic density
STZ
Streptozotocin
T1DM
Type 1 diabetes mellitus
WGCNA
Weighted gene co-expression network analysis

Declarations

Ethical Approval and Consent to participate

To satisfy statistical requirements, we used minimized animals, which were given humane care in accordance with guidelines from the Ethics Committee of animal research of Xi'an Jiaotong University (protocol No. 2019-060). The clinical protocol was approved by the Ethics Committee of the First Affiliated Hospital of Xi'an Jiaotong University (ID: ChiCTR1900021720). All subjects obtained the informed consent of their participation in this study.

Consent for publication

Not applicable

Availability of supporting data

Transcriptomic and proteomic sequencing data that support our findings of this study are original, which are already stored in CNSA (https://db.cngb.org/cnsa/) of CNGBdb (China National GeneBank DataBase) with accession number CNP0002799.

Competing interests

The authors declare no conflicts of interest.

Funding

This study was supported by the National Natural Science Foundation of China (No. 81974540, 81801899, 81971290) and the Fundamental Research Funds for the Central Universities (Grant No. xzy022019020).

Authors' contributions

Qiang Wang, Yansong Li, and Tao Jiang designed this study. Qian Zhai, Chaoying Yan and Zhi Ma contributed to the discussion. Tao Jiang, Kairui Pu, Meiyan Wu, and Mengyu Du performed the study. Shuxuan He, Mengyu Du, and Tao Jiang analyzed the results. Tao Jiang, Yansong Li, and Qiang Wang wrote the manuscript. All authors read and approved the final manuscript.

Acknowledgements

We gratefully acknowledge engineer Ying Hao at the Instrumental Analysis Center of Xi'an Jiaotong University for technical assistance with 3D structure reconstruction of dendritic spines.

Authors' information

Tao Jiang and Yansong Li contributed equally to this work. Correspondence and requests for materials should be addressed to Qiang Wang, Email: dr.wangqiang@mail.xjtu.edu.cn.

References

1. Disease GBD, Injury I, Prevalence C. Global, regional, and national incidence, prevalence, and years lived with disability for 354 diseases and injuries for 195 countries and territories, 1990–2017: a systematic analysis for the Global Burden of Disease Study 2017. Lancet. 2018;392(10159):1789–858.
2. Zilliox LA, Chadrasekaran K, Kwan JY, Russell JW. Diabetes and Cognitive Impairment Curr Diab Rep. 2016;16(9):87.
3. Gao Y, Xiao Y, Miao R, Zhao J, Cui M, Huang G, et al. The prevalence of mild cognitive impairment with type 2 diabetes mellitus among elderly people in China: A cross-sectional study. Arch Gerontol Geriatr. 2016;62:138–42.
4. Biessels GJ, Whitmer RA. Cognitive dysfunction in diabetes: how to implement emerging guidelines. Diabetologia. 2020;63(1):3–9.
5. Biessels GJ, Despa F. Cognitive decline and dementia in diabetes mellitus: mechanisms and clinical implications. Nat Rev Endocrinol. 2018;14(10):591–604.
6. Pearson-Stuttard J, Bennett J, Cheng YJ, Vamos EP, Cross AJ, Ezzati M, et al. Trends in predominant causes of death in individuals with and without diabetes in England from 2001 to 2018: an epidemiological analysis of linked primary care records. Lancet Diabetes Endocrinol. 2021;9(3):165–73.

7. Moon HY, Becke A, Berron D, Becker B, Sah N, Benoni G, et al. Running-Induced Systemic Cathepsin B Secretion Is Associated with Memory Function. Cell Metab. 2016;24(2):332–40.
8. Horowitz AM, Fan X, Bieri G, Smith LK, Sanchez-Diaz CI, Schroer AB, et al. Blood factors transfer beneficial effects of exercise on neurogenesis and cognition to the aged brain. Science. 2020;369(6500):167–73.
9. Lourenco MV, Frozza RL, de Freitas GB, Zhang H, Kincheski GC, Ribeiro FC, et al. Exercise-linked FNDC5/irisin rescues synaptic plasticity and memory defects in Alzheimer's models. Nat Med. 2019;25(1):165–75.
10. Nation DA, Sweeney MD, Montagne A, Sagare AP, D'Orazio LM, Pachicano M, et al. Blood-brain barrier breakdown is an early biomarker of human cognitive dysfunction. Nat Med. 2019;25(2):270–76.
11. Leardini-Tristao M, Andrade G, Garcia C, Reis PA, Lourenco M, Moreira ETS, et al. Physical exercise promotes astrocyte coverage of microvessels in a model of chronic cerebral hypoperfusion. J Neuroinflammation. 2020;17(1):117.
12. Habib N, McCabe C, Medina S, Varshavsky M, Kitsberg D, Dvir-Szternfeld R, et al. Disease-associated astrocytes in Alzheimer's disease and aging. Nat Neurosci. 2020;23(6):701–06.
13. Stogsdill JA, Ramirez J, Liu D, Kim YH, Baldwin KT, Enustun E, et al. Astrocytic neuroligins control astrocyte morphogenesis and synaptogenesis. Nature. 2017;551(7679):192–97.
14. Nagai J, Rajbhandari AK, Gangwani MR, Hachisuka A, Coppola G, Masmanidis SC, et al. Hyperactivity with Disrupted Attention by Activation of an Astrocyte Synaptogenic Cue Cell. 2019;177(5):1280-92 e20.
15. Chung WS, Allen NJ, Eroglu C. Astrocytes Control Synapse Formation, Function, and Elimination. Cold Spring Harb Perspect Biol. 2015;7(9):a020370.
16. Santello M, Toni N, Volterra A. Astrocyte function from information processing to cognition and cognitive impairment. Nat Neurosci. 2019;22(2):154–66.
17. Adamsky A, Kol A, Kreisel T, Doron A, Ozeri-Engelhard N, Melcer T, et al. Astrocytic Activation Generates De Novo Neuronal Potentiation and Memory Enhancement Cell. 2018;174(1):59–71 e14.
18. Yun SP, Kam TI, Panicker N, Kim S, Oh Y, Park JS, et al. Block of A1 astrocyte conversion by microglia is neuroprotective in models of Parkinson's disease. Nat Med. 2018;24(7):931–38.
19. Liddelow SA, Guttenplan KA, Clarke LE, Bennett FC, Bohlen CJ, Schirmer L, et al. Neurotoxic reactive astrocytes are induced by activated microglia. Nature. 2017;541(7638):481–87.
20. Lian H, Yang L, Cole A, Sun L, Chiang AC, Fowler SW, et al. NFkappaB-activated astroglial release of complement C3 compromises neuronal morphology and function associated with Alzheimer's disease. Neuron. 2015;85(1):101–15.
21. Schartz ND, Tenner AJ. The good, the bad, and the opportunities of the complement system in neurodegenerative disease. J Neuroinflammation. 2020;17(1):354.
22. King BC, Blom AM. Complement in metabolic disease: metaflammation and a two-edged sword. Semin Immunopathol. 2021;43(6):829–41.

23. Stokowska A, Atkins AL, Moran J, Pekny T, Bulmer L, Pascoe MC, et al. Complement peptide C3a stimulates neural plasticity after experimental brain ischaemia. Brain. 2017;140(2):353–69.
24. Joshi AU, Minhas PS, Liddelow SA, Haileselassie B, Andreasson KI, Dorn GW 2. Fragmented mitochondria released from microglia trigger A1 astrocytic response and propagate inflammatory neurodegeneration. Nat Neurosci. 2019;22(10):1635–48. nd, et al.
25. Li Y, Yin A, Sun X, Zhang M, Zhang J, Wang P, et al. Deficiency of tumor suppressor NDRG2 leads to attention deficit and hyperactive behavior. J Clin Invest. 2017;127(12):4270–84.
26. Takarada-Iemata M, Yoshikawa A, Ta HM, Okitani N, Nishiuchi T, Aida Y, et al. N-myc downstream-regulated gene 2 protects blood-brain barrier integrity following cerebral ischemia. Glia. 2018;66(7):1432–46.
27. Hu XL, Liu XP, Deng YC, Lin SX, Wu L, Zhang J, et al. Expression analysis of the NDRG2 gene in mouse embryonic and adult tissues. Cell Tissue Res. 2006;325(1):67–76.
28. Li X, Wu X, Luo P, Xiong L. Astrocyte-specific NDRG2 gene: functions in the brain and neurological diseases. Cell Mol Life Sci. 2020;77(13):2461–72.
29. Skiriute D, Steponaitis G, Vaitkiene P, Mikuciunas M, Skauminas K, Tamasauskas A, et al. Glioma Malignancy-Dependent NDRG2 Gene Methylation and Downregulation Correlates with Poor Patient Outcome. J Cancer. 2014;5(6):446–56.
30. Yin A, Guo H, Tao L, Cai G, Wang Y, Yao L, et al. NDRG2 Protects the Brain from Excitotoxicity by Facilitating Interstitial Glutamate Uptake. Transl Stroke Res. 2020;11(2):214–27.
31. Guo H, Yin A, Ma Y, Fan Z, Tao L, Tang W, et al. Astroglial N-myc downstream-regulated gene 2 protects the brain from cerebral edema induced by stroke. Glia. 2021;69(2):281–95.
32. Tao L, Zhu Y, Wang R, Han J, Ma Y, Guo H, et al. N-myc downstream-regulated gene 2 deficiency aggravates memory impairment in Alzheimer's disease. Behav Brain Res. 2020;379:112384.
33. Ichikawa T, Nakahata S, Tamura T, Manachai N, Morishita K. The loss of NDRG2 expression improves depressive behavior through increased phosphorylation of GSK3beta. Cell Signal. 2015;27(10):2087–98.
34. Choi SH, Bylykbashi E, Chatila ZK, Lee SW, Pulli B, Clemenson GD, et al. *Combined adult neurogenesis and BDNF mimic exercise effects on cognition in an Alzheimer's mouse model*. Science. 2018; 361(6406).
35. Moien-Afshari F, Ghosh S, Elmi S, Rahman MM, Sallam N, Khazaei M, et al. Exercise restores endothelial function independently of weight loss or hyperglycaemic status in db/db mice. Diabetologia. 2008;51(7):1327–37.
36. Cheang WS, Wong WT, Zhao L, Xu J, Wang L, Lau CW, et al. PPARdelta Is Required for Exercise to Attenuate Endoplasmic Reticulum Stress and Endothelial Dysfunction in Diabetic Mice. Diabetes. 2017;66(2):519–28.
37. Li J, Liu B, Cai M, Lin X, Lou S. Glucose metabolic alterations in hippocampus of diabetes mellitus rats and the regulation of aerobic exercise. Behav Brain Res. 2019;364:447–56.

38. Swarup V, Chang TS, Duong DM, Dammer EB, Dai J, Lah JJ, et al. Identif Conserved Proteomic Networks Neurodegenerative Dement Cell Rep. 2020;31(12):107807.
39. Wisniewski JR, Zougman A, Nagaraj N, Mann M. Universal sample preparation method for proteome analysis. Nat Methods. 2009;6(5):359–62.
40. Zhu Y, Xu H, Chen H, Xie J, Shi M, Shen B, et al. Proteomic analysis of solid pseudopapillary tumor of the pancreas reveals dysfunction of the endoplasmic reticulum protein processing pathway. Mol Cell Proteomics. 2014;13(10):2593–603.
41. Di Liberto G, Pantelyushin S, Kreutzfeldt M, Page N, Musardo S, Coras R, et al. Neurons under T Cell Attack Coordinate Phagocyte-Mediated Synaptic Stripping. Cell. 2018;175(2):458–71. e19.
42. Wu S, Lu Q, Ding Y, Wu Y, Qiu Y, Wang P, et al. Hyperglycemia-Driven Inhibition of AMP-Activated Protein Kinase alpha2 Induces Diabetic Cardiomyopathy by Promoting Mitochondria-Associated Endoplasmic Reticulum Membranes In Vivo. Circulation. 2019;139(16):1913–36.
43. Fidler TP, Marti A, Gerth K, Middleton EA, Campbell RA, Rondina MT, et al. Glucose Metabolism Is Required for Platelet Hyperactivation in a Murine Model of Type 1 Diabetes. Diabetes. 2019;68(5):932–38.
44. Kronlage M, Dewenter M, Grosso J, Fleming T, Oehl U, Lehmann LH, et al. O-GlcNAcylation of Histone Deacetylase 4 Protects the Diabetic Heart From Failure. Circulation. 2019;140(7):580–94.
45. Kleinert M, Clemmensen C, Hofmann SM, Moore MC, Renner S, Woods SC, et al. Animal models of obesity and diabetes mellitus. Nat Rev Endocrinol. 2018;14(3):140–62.
46. Rom S, Zuluaga-Ramirez V, Gajghate S, Seliga A, Winfield M, Heldt NA, et al. Hyperglycemia-Driven Neuroinflammation Compromises BBB Leading to Memory Loss in Both Diabetes Mellitus (DM) Type 1 and Type 2 Mouse Models. Mol Neurobiol. 2019;56(3):1883–96.
47. Ramos-Rodriguez JJ, Ortiz O, Jimenez-Palomares M, Kay KR, Berrocoso E, Murillo-Carretero MI, et al. Differential central pathology and cognitive impairment in pre-diabetic and diabetic mice. Psychoneuroendocrinology. 2013;38(11):2462–75.
48. Lee JH, Kim JY, Noh S, Lee H, Lee SY, Mun JY, et al. Astrocytes phagocytose adult hippocampal synapses for circuit homeostasis. Nature. 2021;590(7847):612–17.
49. Owen B, Bichler E, Benveniste M. Excitatory synaptic transmission in hippocampal area CA1 is enhanced then reduced as chronic epilepsy progresses. Neurobiol Dis. 2021;154:105343.
50. Matzeu A, Kallupi M, George O, Schweitzer P, Martin-Fardon R. Dynorphin Counteracts Orexin in the Paraventricular Nucleus of the Thalamus: Cellular and Behavioral Evidence. Neuropsychopharmacology. 2018;43(5):1010–20.
51. Leinenga G, Gotz J. Scanning ultrasound removes amyloid-beta and restores memory in an Alzheimer's disease mouse model. Sci Transl Med. 2015;7(278):278ra33.
52. Ye T, Meng X, Wang R, Zhang C, He S, Sun G, et al. *Gastrodin Alleviates Cognitive Dysfunction and Depressive-Like Behaviors by Inhibiting ER Stress and NLRP3 Inflammasome Activation in db/db Mice*. Int J Mol Sci. 2018; 19(12).

53. Kivipelto M, Mangialasche F, Ngandu T. Lifestyle interventions to prevent cognitive impairment, dementia and Alzheimer disease. Nat Rev Neurol. 2018;14(11):653–66.
54. Cukierman-Yaffe T, Gerstein HC, Colhoun HM, Diaz R, Garcia-Perez LE, Lakshmanan M, et al. Effect of dulaglutide on cognitive impairment in type 2 diabetes: an exploratory analysis of the REWIND trial. Lancet Neurol. 2020;19(7):582–90.
55. Johnson ECB, Dammer EB, Duong DM, Ping L, Zhou M, Yin L, et al. Large-scale proteomic analysis of Alzheimer's disease brain and cerebrospinal fluid reveals early changes in energy metabolism associated with microglia and astrocyte activation. Nat Med. 2020;26(5):769–80.
56. Bereczki E, Branca RM, Francis PT, Pereira JB, Baek JH, Hortobagyi T, et al. Synaptic markers of cognitive decline in neurodegenerative diseases: a proteomic approach. Brain. 2018;141(2):582–95.
57. Vasek MJ, Garber C, Dorsey D, Durrant DM, Bollman B, Soung A, et al. A complement-microglial axis drives synapse loss during virus-induced memory impairment. Nature. 2016;534(7608):538–43.
58. Propson NE, Gedam M, Zheng H. Complement in Neurologic Disease. Annu Rev Pathol. 2021;16:277–98.
59. Xin W, Chan JR. That Wasn't a Complement-Too Much C3 in Demyelinating Disease. Immunity. 2020;52(1):11–3.
60. Liu Z, Dai X, Zhang H, Shi R, Hui Y, Jin X, et al. Gut microbiota mediates intermittent-fasting alleviation of diabetes-induced cognitive impairment. Nat Commun. 2020;11(1):855.
61. Huang S, Wang Y, Gan X, Fang D, Zhong C, Wu L, et al. Drp1-mediated mitochondrial abnormalities link to synaptic injury in diabetes model. Diabetes. 2015;64(5):1728–42.
62. Zhao Y, Luo C, Chen J, Sun Y, Pu D, Lv A, et al. High glucose-induced complement component 3 up-regulation via RAGE-p38MAPK-NF-kappaB signalling in astrocytes: In vivo and in vitro studies. J Cell Mol Med. 2018;22(12):6087–98.
63. Flugge G, Araya-Callis C, Garea-Rodriguez E, Stadelmann-Nessler C, Fuchs E. NDRG2 as a marker protein for brain astrocytes. Cell Tissue Res. 2014;357(1):31–41.
64. Zhang Z, Ma Z, Zou W, Zhang L, Li Y, Zhang J, et al. N-myc downstream-regulated gene 2 controls astrocyte morphology via Rho-GTPase signaling. J Cell Physiol. 2019;234(11):20847–58.
65. Zahir F, Firth HV, Baross A, Delaney AD, Eydoux P, Gibson WT, et al. Novel deletions of 14q11.2 associated with developmental delay, cognitive impairment and similar minor anomalies in three children. J Med Genet. 2007;44(9):556–61.
66. Wei Y, Chen T, Bosco DB, Xie M, Zheng J, Dheer A, et al. The complement C3-C3aR pathway mediates microglia-astrocyte interaction following status epilepticus. Glia. 2021;69(5):1155–69.
67. McCrimmon RJ, Ryan CM, Frier BM. Diabetes and cognitive dysfunction. Lancet. 2012;379(9833):2291–9.
68. Wu T, Dejanovic B, Gandham VD, Gogineni A, Edmonds R, Schauer S, et al. Complement C3 Is Activated in Human AD Brain and Is Required for Neurodegeneration in Mouse Models of Amyloidosis and Tauopathy. Cell Rep. 2019;28(8):2111–23. e6.

69. Litvinchuk A, Wan YW, Swartzlander DB, Chen F, Cole A, Propson NE, et al. Complement C3aR Inactivation Attenuates Tau Pathology and Reverses an Immune Network Deregulated in Tauopathy Models and Alzheimer's Disease. Neuron. 2018; 100(6): 1337–53 e5.

70. Yu H, Li H, Liu X, Du X, Deng B. Levels of serum S100B are associated with cognitive dysfunction in patients with type 2 diabetes. Aging. 2020;12(5):4193–203.

Figures

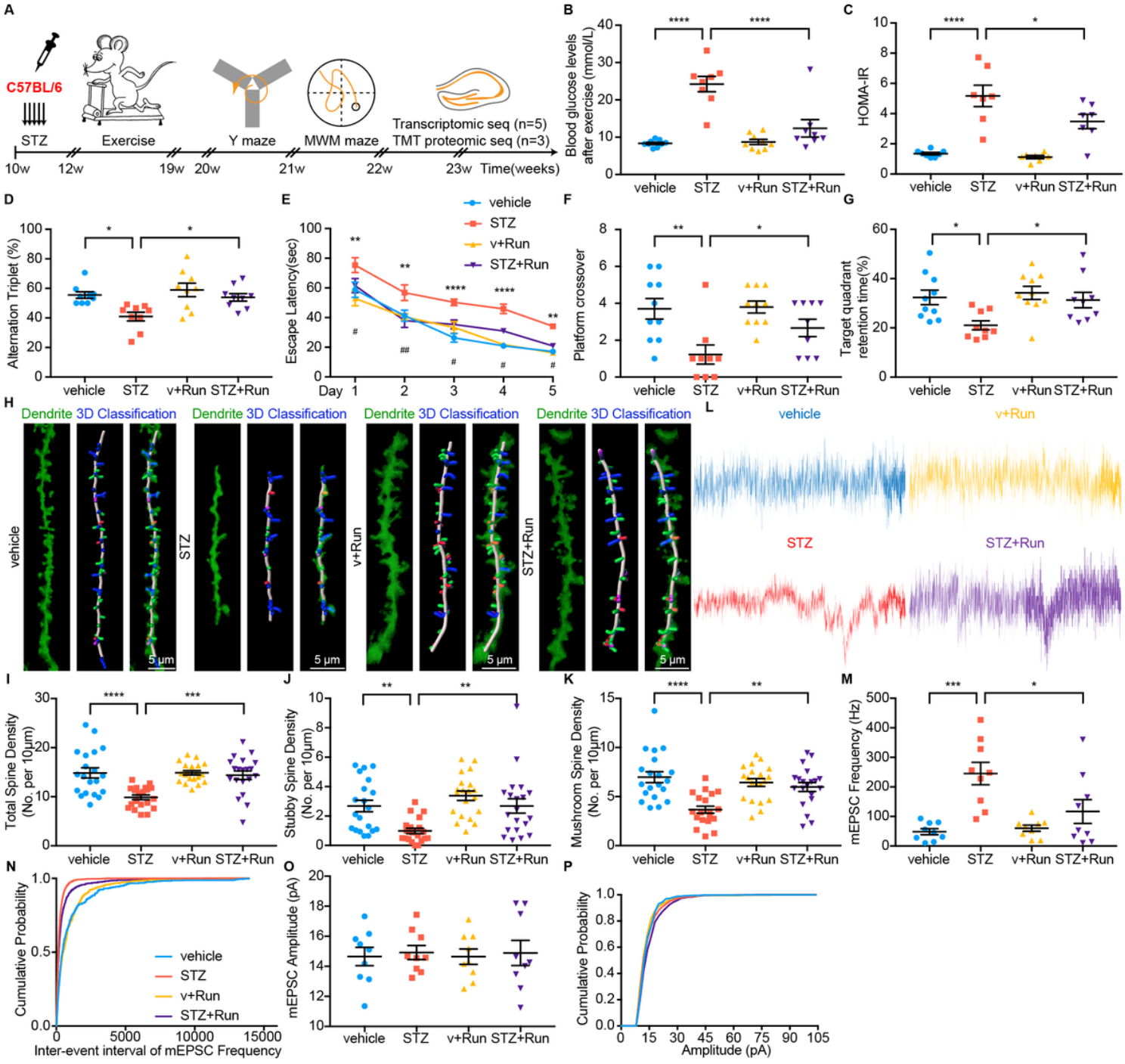

Figure 1

The alteration of neuronal synaptic plasticity and cognitive deficits in diabetic mice. (A) Schematic that represents chronological order of STZ injection, exercise, cognitive testing, and omics analysis. **(B)** The random blood glucose levels after exercise (n=9 mice for the vehicle and v+Run groups, n=8 mice for the STZ and STZ+Run groups, ****P < 0.0001, two-sided one-way ANOVA with Tukey's multiple comparisons test). **(C)** HOMA-IR after exercise (n=8 mice for the vehicle group, n=7 mice for the v+Run, STZ, and STZ+Run groups, *P < 0.05, ****P < 0.0001, two-sided one-way ANOVA with Tukey's multiple comparisons test). **(D)** Y-maze alternation triplet (%) (n=9 mice per group, *P < 0.05, two-sided one-way ANOVA with Tukey's multiple comparisons test). **(E)** Escape latency for the MWM test (n=10 mice for the vehicle and v+Run groups, n=9 mice for the STZ and STZ+Run groups, **P < 0.01, ****P < 0.0001 vehicle vs. STZ, $^{\#}$P < 0.05, $^{\#\#}$P < 0.01 STZ vs. STZ+Run, two-sided two-way ANOVA with Tukey's multiple comparisons test). **(F-G)** The platform crossover (**F**) and target quadrant retention time (%) (**G**) during the probe trial of the MWM test (n=10 mice for the vehicle and v+Run groups, n=9 mice for the STZ and STZ+Run groups, *P < 0.05, **P < 0.01, two-sided one-way ANOVA with Tukey's multiple comparisons test). **(H)** Representative images of dendritic spine 3D reconstruction to classify stubby, mushroom, long thin, and filopodia spines. Scale bar, 5 μm. **(I-K)** The densities of total spines (**I**), stubby spines (**J**), and mushroom spines (**K**) (n=20 dendrites from three animals per group. **P < 0.01, ***P < 0.001, ****P < 0.0001, two-sided one-way ANOVA with Tukey's multiple comparisons test). **(L)** Representative images of mEPSC traces in CA1 pyramidal neurons. **(M, O)** Average neuron mEPSC frequency (**M**) and amplitude (**O**) (n=9 cells from three animals per group, *P < 0.05, ***P < 0.001, two-sided one-way ANOVA with Tukey's multiple comparisons test). **(N, P)** Cumulative distributions of mEPSC frequency (**N**) and amplitude (**P**) (n=9 cells from three animals per group). Data are presented as mean ± SEM.

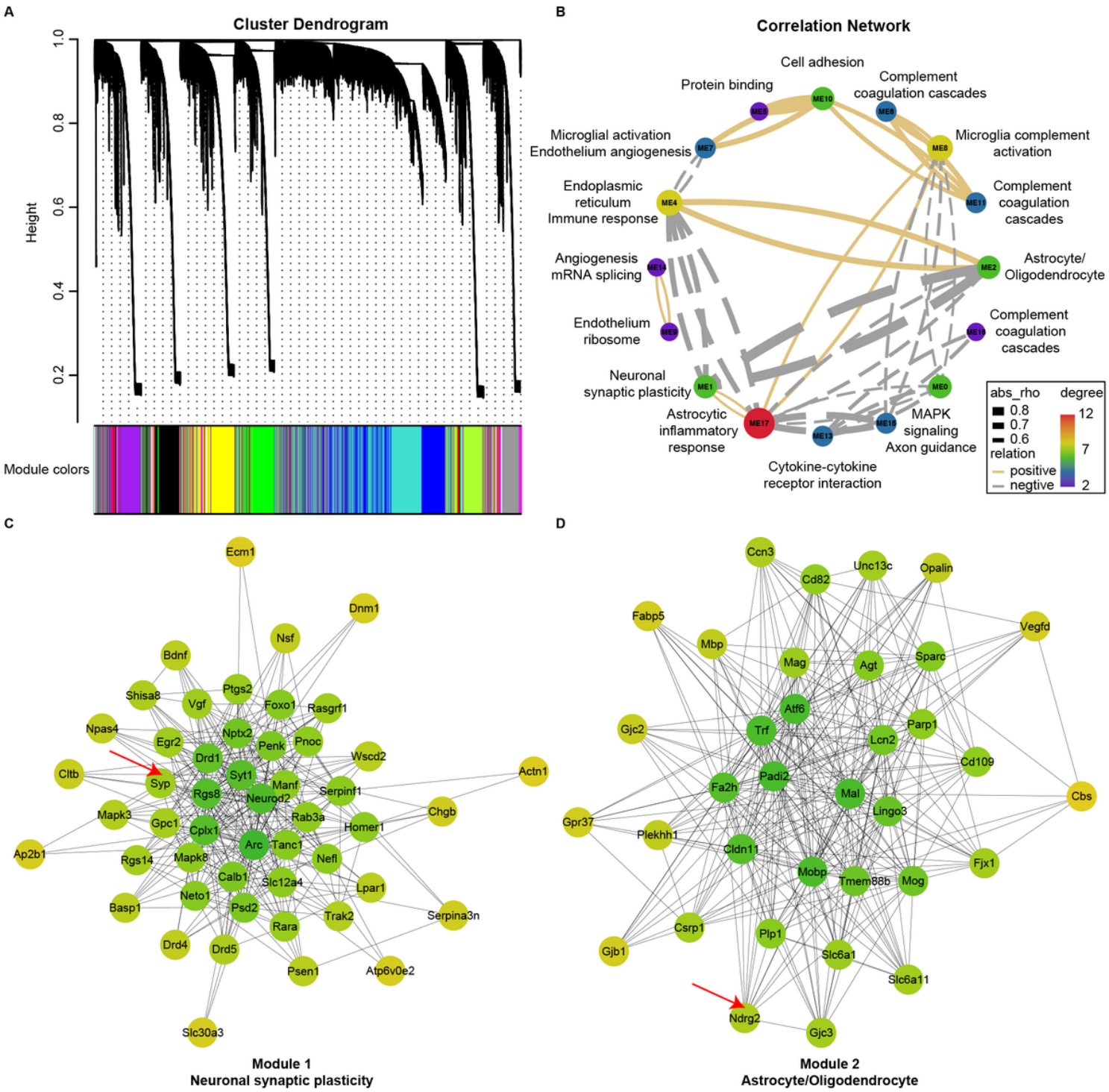

Figure 2

Transcriptomic analysis revealed the integrative pathogenesis of DACD. (A) Cluster dendrogram of WGCNA in transcriptome showing the 18 modules, which are distinguished by different colors (n=5 mice per group). **(B)** Correlation network that demonstrates the major cell-types and Gene Ontology enrichments for each module and the relationships from a multidimensional perspective. Yellow represents positive correlation, and grey represents negative correlation. **(C)** Module 1 enriched neuronal synaptic plasticity genes: Syt1, Manf, Syp, and Bdnf. **(D)** Astrocytic and oligodendrocytic genes (Ndrg2, Lcn2, and Mobp) were enriched in module 2.

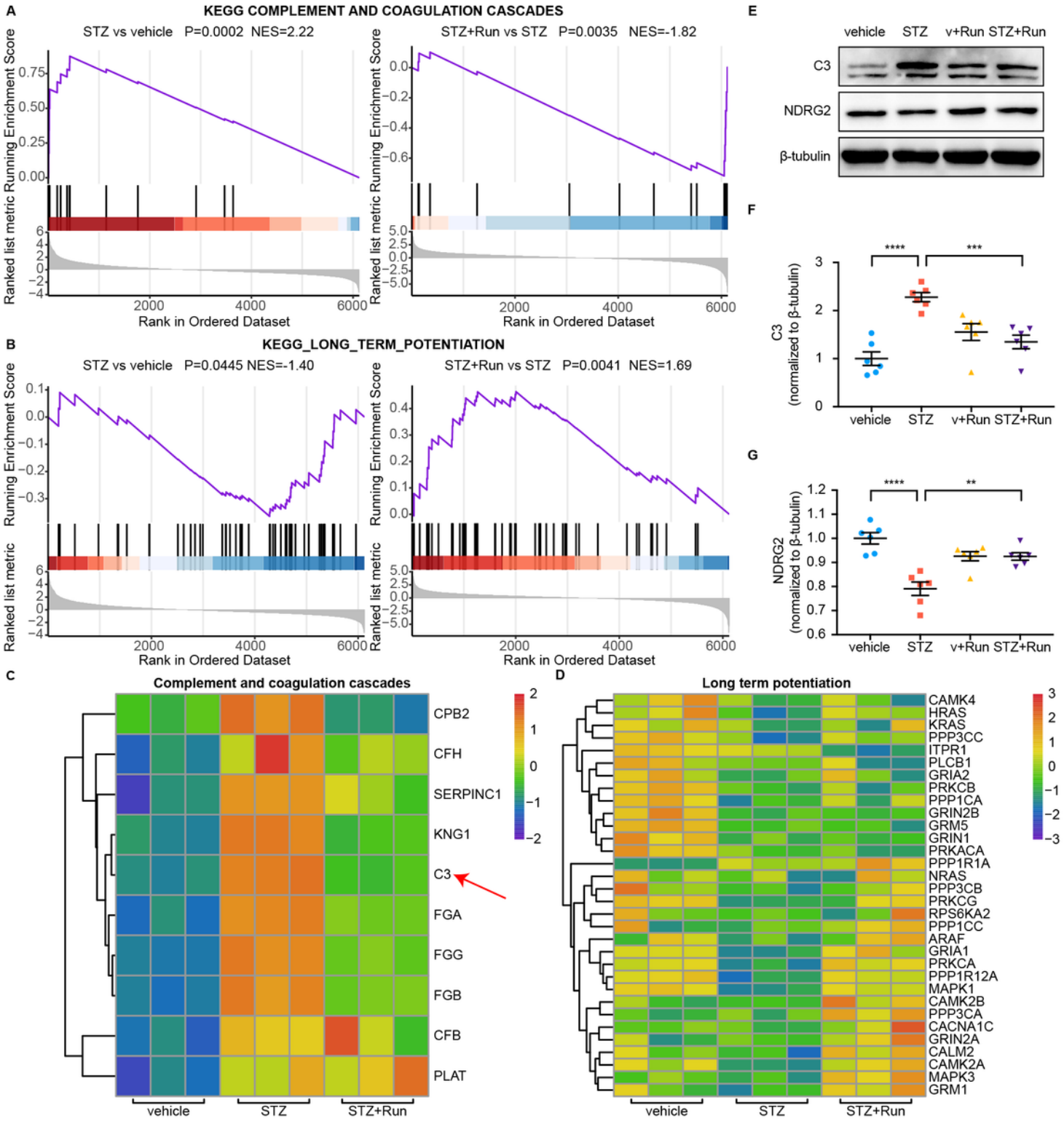

Figure 3

Proteomic analysis revealed astrocytic NDRG2/C3 has vital role in neuronal synaptic plasticity. (A) GSEA of proteome indicated complement and coagulation cascade signaling were upregulated in diabetic mice and downregulated after exercise. The cumulative enrichment scores were normalized (NES) (n=3 mice per group). **(B)** GSEA of proteome demonstrated that long-term potentiation protein levels were decreased in diabetic mice and increased after exercise (n=3 mice per group). **(C-D)** Heatmaps showing the fold

changes of significantly altered proteins in complement and coagulation cascades (**C**) and long-term potentiation pathways (**D**) (n=3 mice per group). **(E-G)** Representative immunoblots of complement C3 (**E**, **F**) and astrocytic NDRG2 (**G**) in the hippocampus (n=6 mice per group, **P < 0.01, ***P < 0.001, ****P < 0.0001, two-sided one-way ANOVA with Tukey's multiple comparisons test). Data are presented as mean ± SEM.

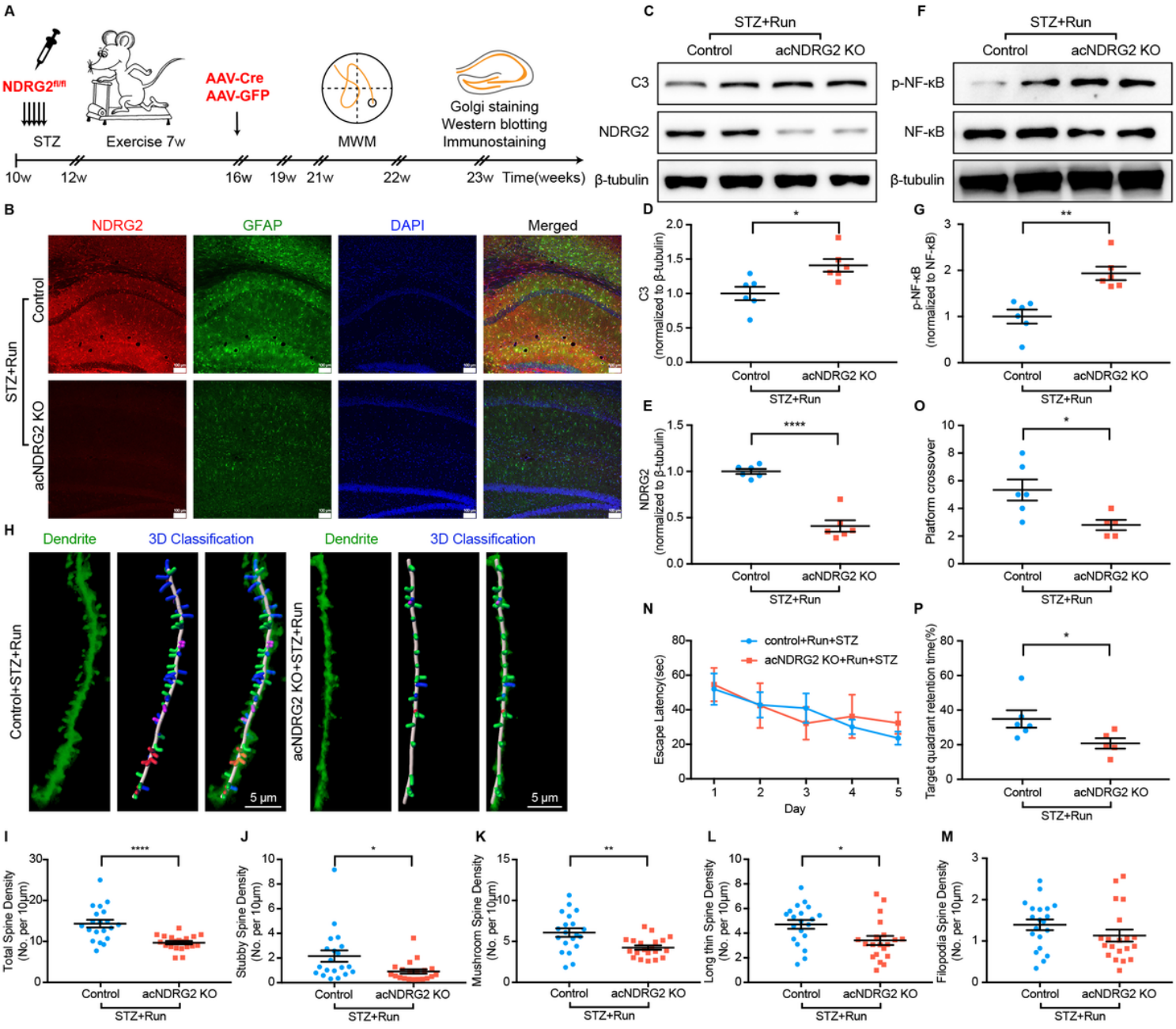

Figure 4

NDRG2 deficiency aggravated dendritic spine loss and cognitive dysfunction by activating p-NF-κB/C3 signaling. (A) Schematic representing chronological order of STZ injection, exercise, AAV-Cre to induce NDRG2 deficiency, and behavioral testing. **(B)** Representative microscopic fields of NDRG2 deficiency in the hippocampus. Red: NDRG2, green: GFAP, blue: DAPI. Scale bar, 100 μm. **(C-G)** Representative

immunoblots of complement C3 (**C, D**), astrocytic NDRG2 (**C, E**), NF-κB, and p-NF-κB (**F, G**) in the hippocampus (n=6 mice per group, *P < 0.05, **P < 0.01, ****P < 0.0001, two-sided one-way ANOVA with Tukey's multiple comparisons test). **(H)** Representative images of dendritic spine 3D reconstruction in the acNDRG2 KO+Run+STZ and control+Run+STZ mice. Scale bar, 5 μm. **(I-M)** The densities of total spines (**I**), stubby spines (**J**), mushroom spines (**K**), long thin spines (**L**), and filopodia spines (**M**) (n=20 dendrites from three animals per group. *P < 0.05, **P < 0.01, ****P < 0.0001, two-sided one-way ANOVA with Tukey's multiple comparisons test). **(N-P)** The escape latency (**N**), platform crossover (**O**), and target quadrant retention time (%) (**P**) for MWM tests (n=6 mice for the control+Run+STZ group, n=5 mice for the acNDRG2 KO+Run+STZ group, *P < 0.05, two-sided one-way ANOVA with Tukey's multiple comparisons test). Data are presented as mean ± SEM.

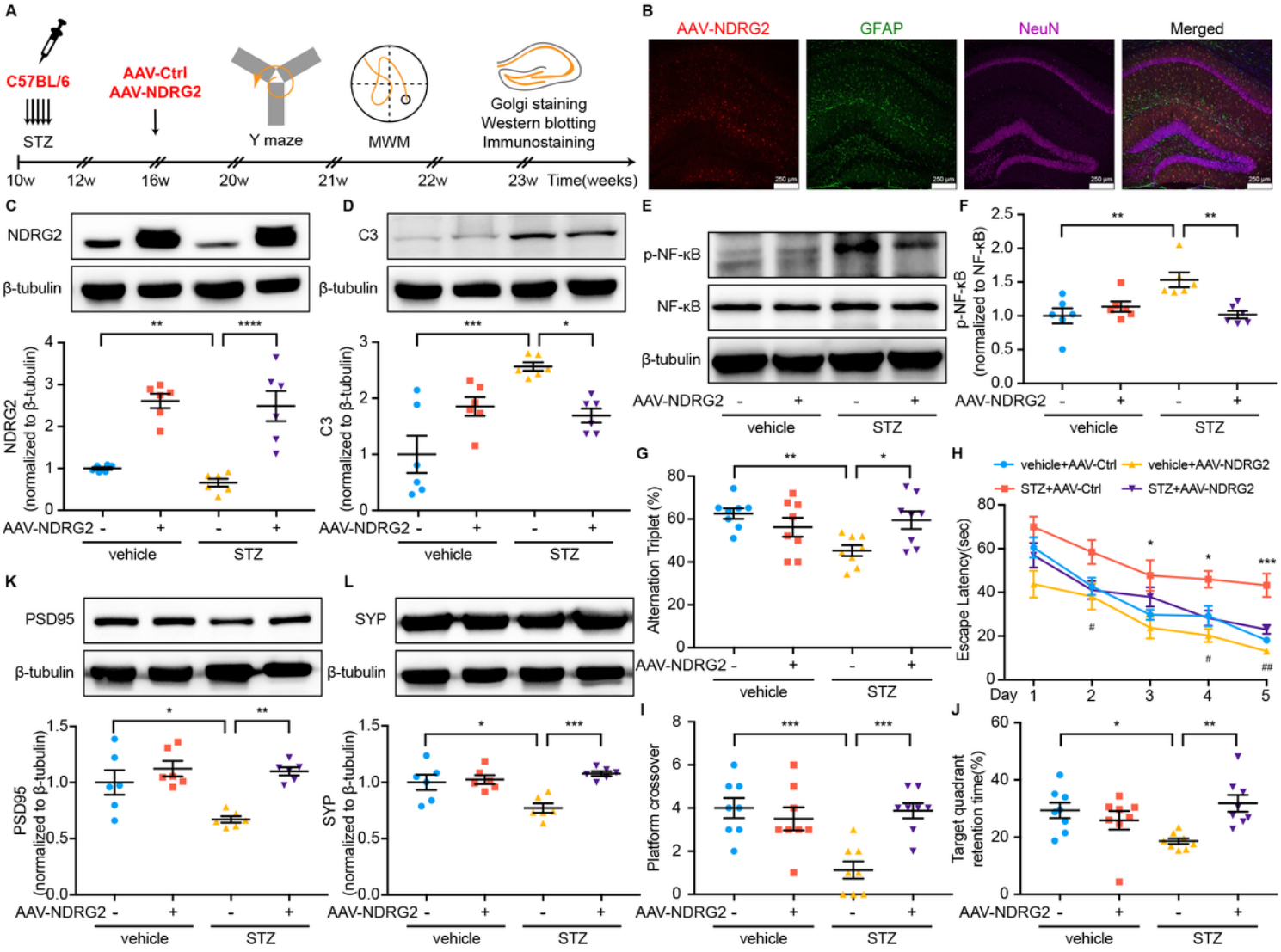

Figure 5

The protective effect of NDRG2 in alleviating synaptic injury and memory deficits by inhibiting p-NF-κB/C3 signaling. (A) Schematic representing chronological order of STZ injection, NDRG2 overexpression,

and behavioral testing. **(B)** Representative immunofluorescent staining of NDRG2 overexpression in the hippocampus. Red: NDRG2, green: GFAP, purple: NeuN, blue: DAPI. Scale bar, 250 μm. **(C-F)** Representative immunoblots of astrocytic NDRG2 (**C**), complement C3 (**D**), NF-κB, and p-NF-κB (**E,F**) (n=6 mice per group, *P < 0.05, **P < 0.01, ***P < 0.0001, ****P < 0.0001, two-sided one-way ANOVA with Tukey's multiple comparisons test). **(G)** Y-maze alternation triplet (%) (n=8 mice per group, *P < 0.05, **P < 0.01, two-sided one-way ANOVA with Tukey's multiple comparisons test). **(H)** Escape latency for the MWM test (n=8 mice per group, *P < 0.05, ***P < 0.001, vehicle+AAV-Ctrl vs. STZ+AAV-Ctrl, $^{\#}$P < 0.05, $^{\#\#}$P < 0.01, STZ+AAV-Ctrl vs. STZ+AAV-NDRG2, two-sided two-way ANOVA with Tukey's multiple comparisons test). **(I-J)** The platform crossover (**I**) and target quadrant retention time (%) (**J**) during the probe trial of the MWM test (n=8 mice per group, *P < 0.05, **P < 0.01, ***P < 0.001, two-sided one-way ANOVA with Tukey's multiple comparisons test). **(K-L)** Representative immunoblots of synaptic proteins: PSD95 (**K**) and SYP (**L**) (n=6 mice per group, *P < 0.05, **P < 0.01, ***P < 0.001, two-sided one-way ANOVA with Tukey's multiple comparisons test). Data are presented as mean ± SEM.

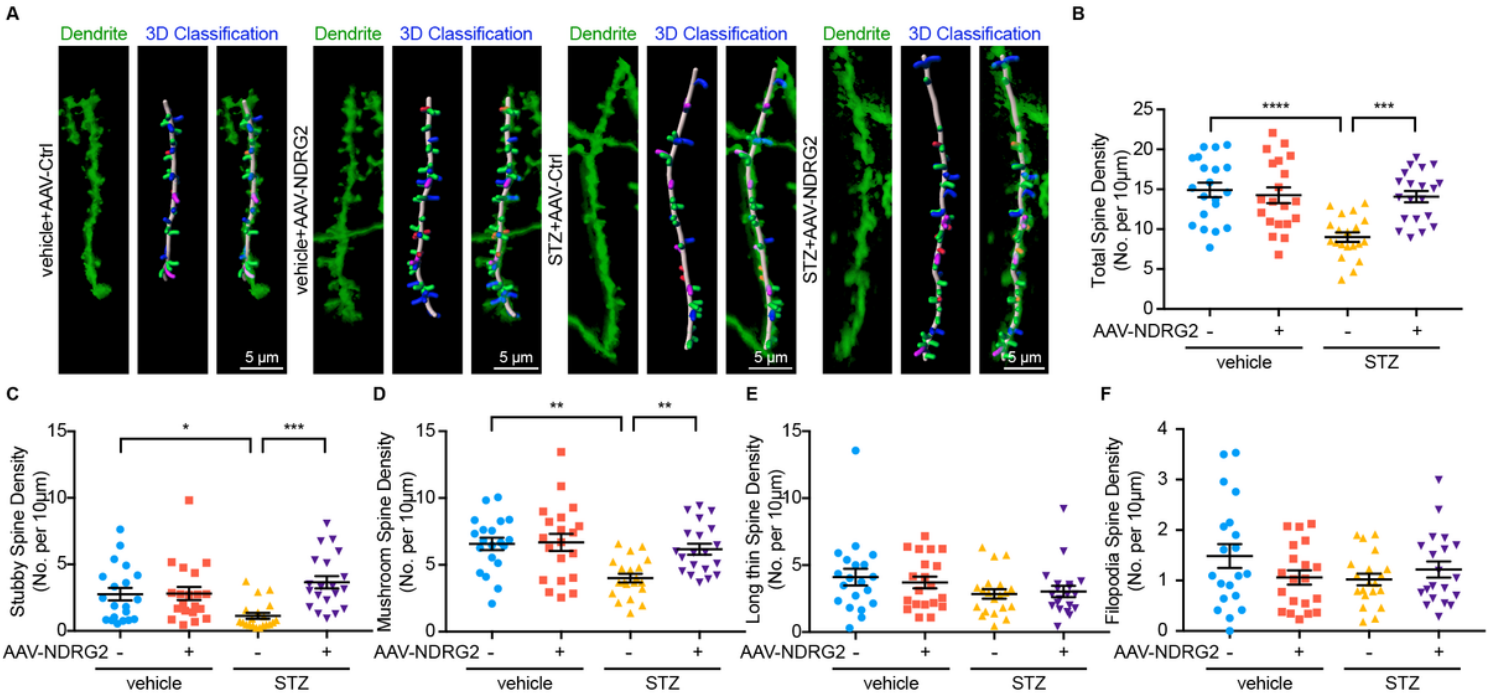

Figure 6

NDRG2 overexpression prevented dendritic spines loss in diabetic mice. (A) Representative images of 3D reconstruction of dendritic spines. Scale bar, 5 μm. **(B-D)** The densities of total spines (**B**), stubby spines (**C**), and mushroom spines (**D**) (n=20 dendrites from three animals per group. *P < 0.05, **P < 0.01, ***P < 0.001, ****P < 0.0001, two-sided one-way ANOVA with Tukey's multiple comparisons test). **(E-F)** The densities of long thin spines (**E**) and filopodia spines (**F**) (n=20 dendrites from three animals per group).

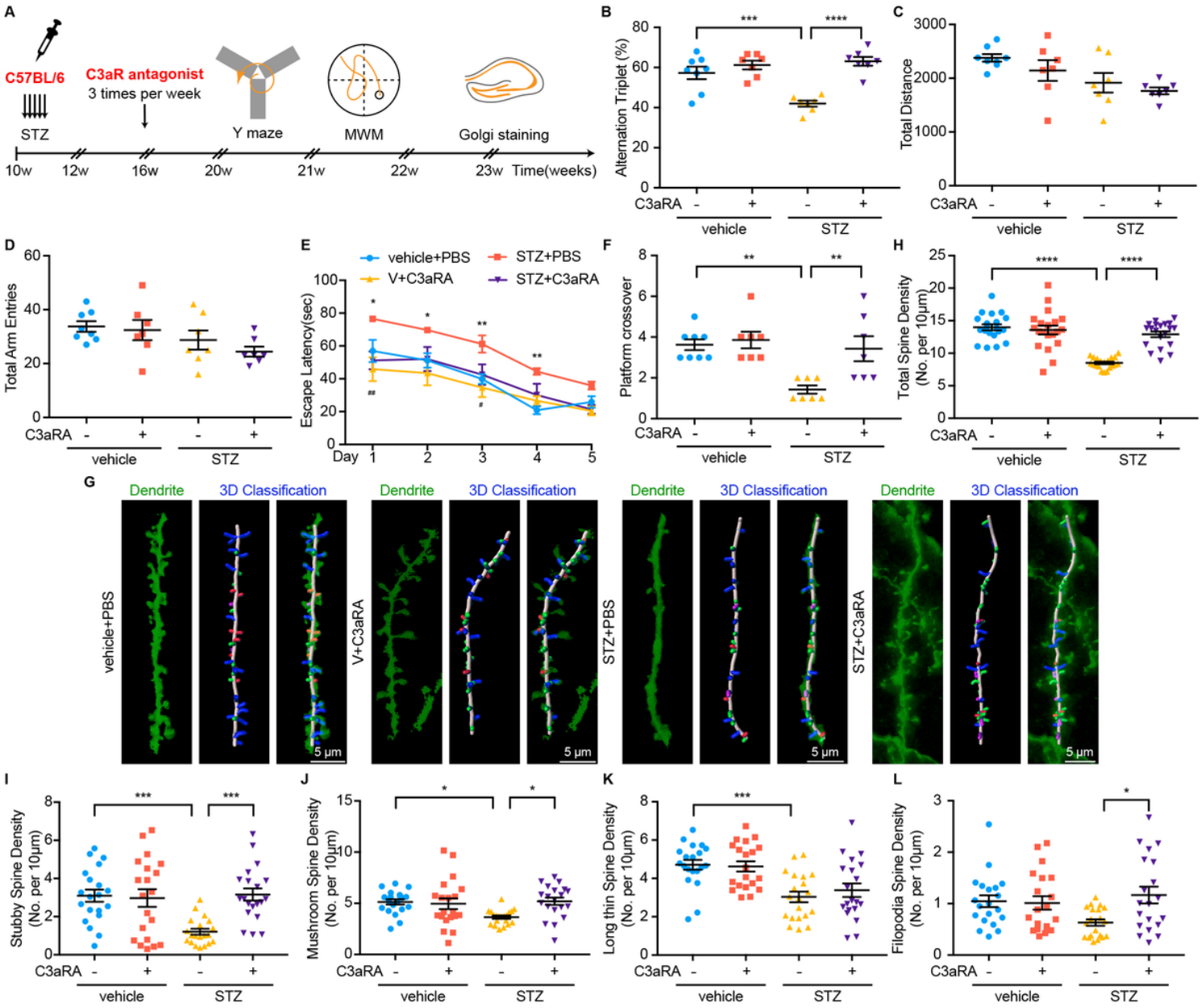

Figure 7

C3aR blockade rescues dendritic spine loss and cognitive dysfunction in diabetic mice. (A) Schematic representing chronological order of STZ injection, C3aR antagonist, and behavioral testing. **(B-D)** Y-maze alternation triplet (%) (**B**), total distance (**C**), and total arm entries (**D**) (n=8 mice for the vehicle+PBS group, n=7 mice for all other groups, ***P < 0.001, ****P < 0.0001, two-sided one-way ANOVA with Tukey's multiple comparisons test). **(E)** Escape latency for the MWM test (n=8 mice for the vehicle+PBS group, n=7 mice for all other groups, *P < 0.05, **P < 0.01, vehicle+PBS vs. STZ+PBS, $^{\#}$P < 0.05, $^{\#\#}$P < 0.01, STZ+PBS vs. STZ+C3aRA, two-sided two-way ANOVA with Tukey's multiple comparisons test). **(F)** Platform crossover during the probe trial of the MWM test (n=8 mice for the vehicle+PBS group, n=7 mice for all other groups, **P < 0.01, two-sided one-way ANOVA with Tukey's multiple comparisons test). **(G)** Representative images of 3D reconstruction of dendritic spines. Scale bar, 5 μm. **(H-L)** The densities of total spines (**H**), stubby spines (**I**), mushroom spines (**J**), long thin spines (**K**), and filopodia spines (**L**)

(n=20 dendrites from three animals per group. *P < 0.05, ***P < 0.001, ****P < 0.0001, two-sided one-way ANOVA with Tukey's multiple comparisons test). Values presented as mean ± SEM.

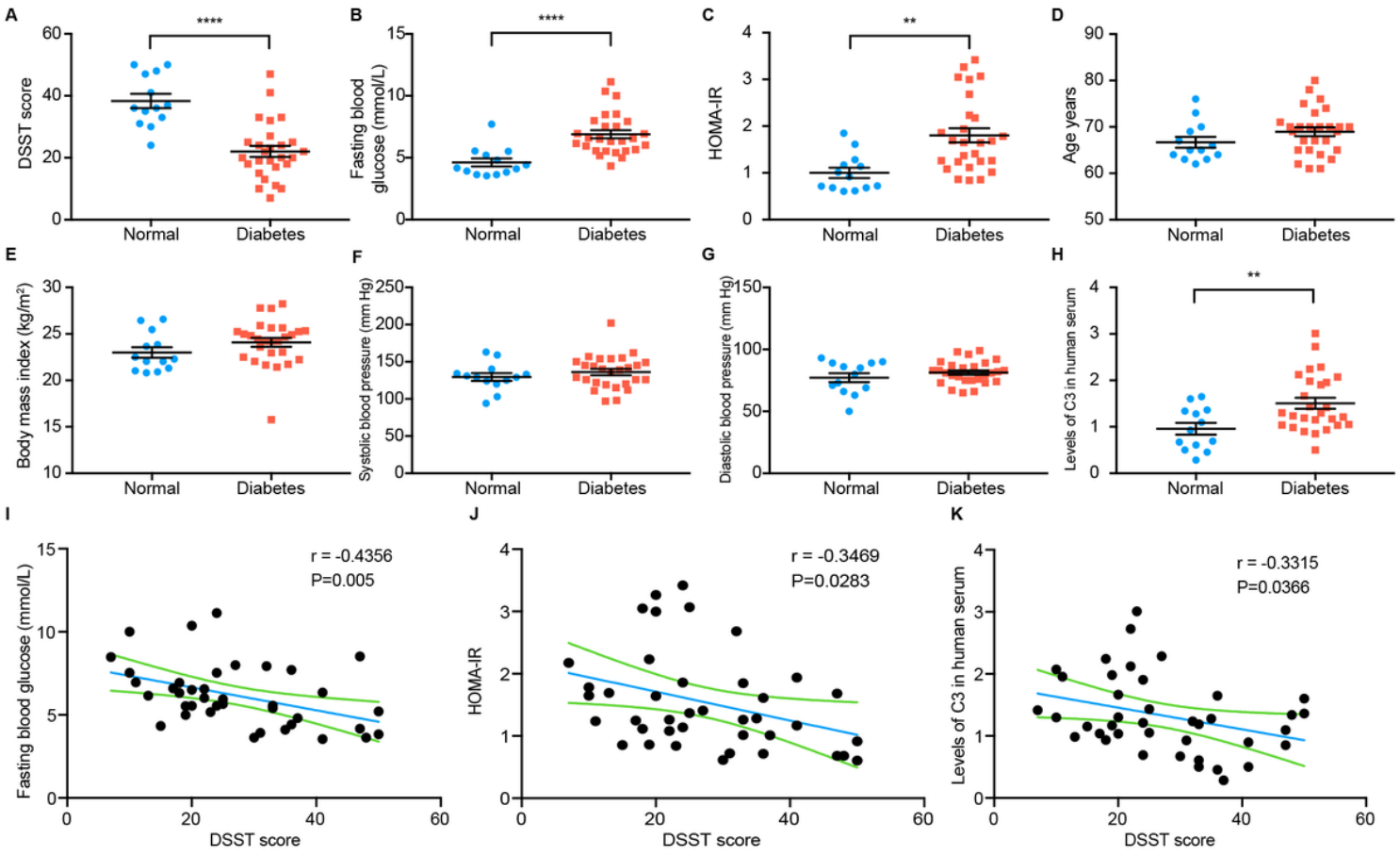

Figure 8

The correlations between various risk factors and cognitive DSST scores in diabetic patients. (A) The DSST scores of diabetic patients (n=27) and non-diabetic peers (n=13) (****P < 0.0001, two-sided unpaired Student's t-test). **(B)** Fasting blood glucose levels for diabetic patients (n=27) compared to non-diabetic patients (n=13) (****P < 0.0001, two-sided unpaired Student's t-test). **(C)** The insulin resistance index HOMA-IR for diabetic patients (n=27) and non-diabetic peers (n=13) (**P < 0.01, two-sided unpaired Student's t-test). **(D-G)** The age (**D**), BMI (**E**), systolic blood pressure (**F**), and diastolic blood pressure (**G**) in diabetic patients (n=27) and non-diabetic peers (n=13). **(H)** The serum levels of complement C3 in diabetic patients (n=27) and normal peers (n=13) (**P < 0.01, two-sided unpaired Student's t-test). **(I-K)** The correlations between DSST score and fasting blood glucose (**I**), HOMA-IR (**J**), and increased C3 levels (**K**) in diabetic patients (n=27) and normal peers (n=13). Correlations were found using linear regression, with r and P values as indicated. Data are presented as mean ± SEM.

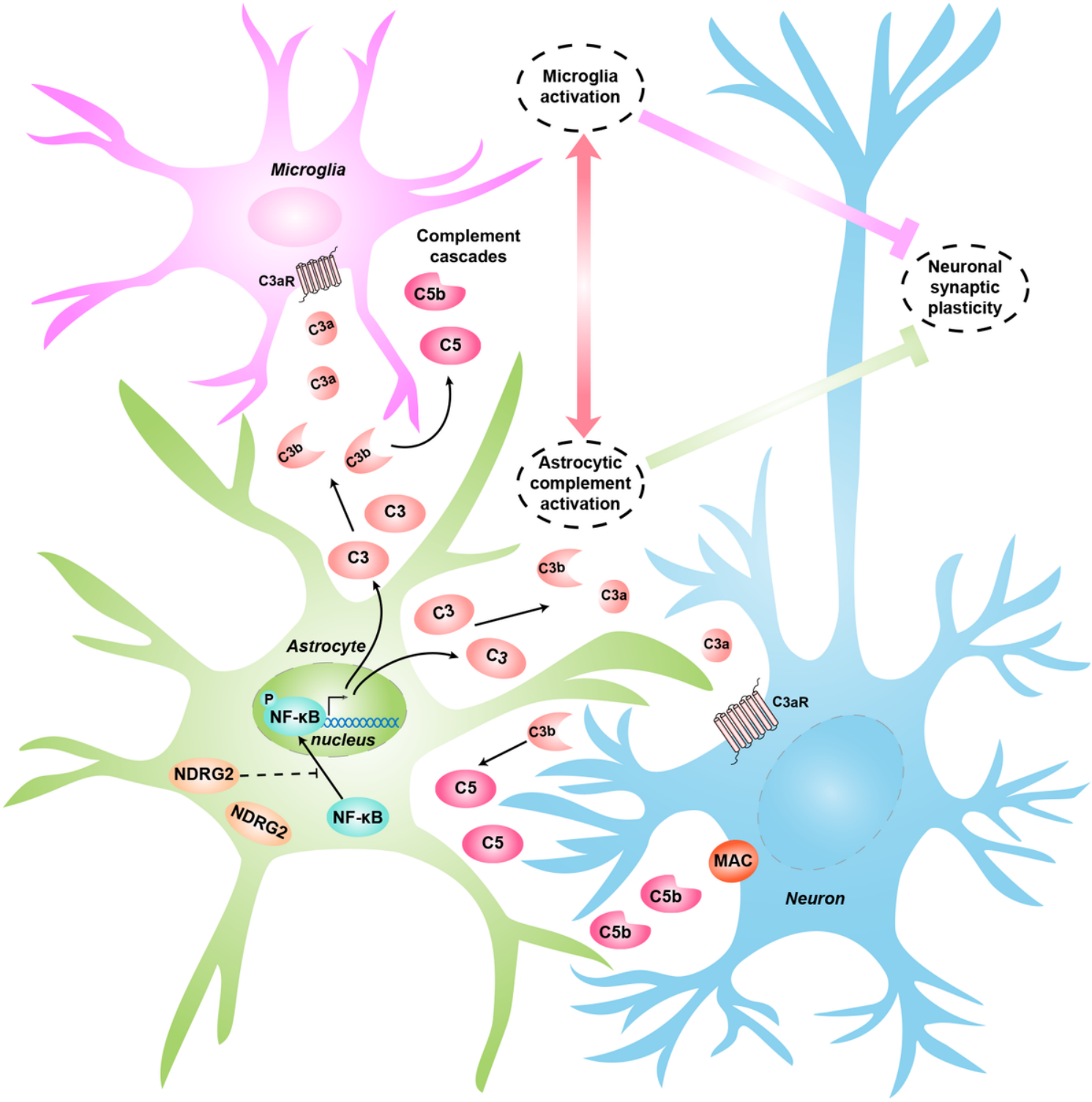

Figure 9

The integrative mechanism of astrocytic NDRG2 and complement cascades in regulating neuronal synaptic plasticity.

Supplementary Files

This is a list of supplementary files associated with this preprint. Click to download.

- SupplementaryInformation.pdf